Submitted to ApJ
Preprint typeset using LaTeX style emulateapj v. 11/10/09

OPTICAL REDSHIFT AND RICHNESS ESTIMATES FOR GALAXY CLUSTERS SELECTED WITH THE SUNYAEV-ZEL'DOVICH EFFECT FROM 2008 SOUTH POLE TELESCOPE OBSERVATIONS

F. W. High,[1] B. Stalder,[1] J. Song,[2] P. A. R. Ade,[3] K. A. Aird,[4] S. S. Allam,[5] R. Armstrong,[6] W. A. Barkhouse,[7] B. A. Benson,[8,9,10] E. Bertin,[11] S. Bhattacharya,[12] L. E. Bleem,[9,13] M. Brodwin,[14] E. J. Buckley-Geer,[5] J. E. Carlstrom,[9,10,13,15] P. Challis,[14] C. L. Chang,[9,10] T. M. Crawford,[9,15] A. T. Crites,[9,15] T. de Haan,[16] S. Desai,[6] M. A. Dobbs,[16] J. P. Dudley,[16] R. J. Foley,[14] E. M. George,[8] M. Gladders,[9,15] N. W. Halverson,[17] M. Hamuy,[18] S. M. Hansen,[19] G. P. Holder,[16] W. L. Holzapfel,[8] J. D. Hrubes,[4] M. Joy,[20] R. Keisler,[9,13] A. T. Lee,[8,21] E. M. Leitch,[9,15] H. Lin,[5] Y.-T. Lin,[22] A. Loehr,[14] M. Lueker,[8] D. Marrone,[4,9] J. J. McMahon,[9,10,23] J. Mehl,[9,15] S. S. Meyer,[9,10,13,15] J. J. Mohr,[24,25,26] T. E. Montroy,[27] N. Morell,[18] C.-C. Ngeow,[2] S. Padin,[9,15] T. Plagge,[8,15] C. Pryke,[9,10,15] C. L. Reichardt,[8] A. Rest,[1] J. Ruel,[1] J. E. Ruhl,[27] K. K. Schaffer,[9,10] L. Shaw,[16,28] E. Shirokoff,[8] R. C. Smith,[29] H. G. Spieler,[21] Z. Staniszewski,[27] A. A. Stark,[14] C. W. Stubbs,[1,14] D. L. Tucker,[5] K. Vanderlinde,[16] J. D. Vieira,[9,13] R. Williamson,[9,15] W. M. Wood-Vasey,[30] Y. Yang,[2] O. Zahn,[8] and A. Zenteno[24,25]

Submitted to ApJ

ABSTRACT

We present redshifts and optical richness properties of 21 galaxy clusters uniformly selected by their Sunyaev-Zel'dovich signature. These clusters, plus an additional, unconfirmed candidate, were detected in a 178 $\deg^2$ area surveyed by the South Pole Telescope in 2008. Using *griz* imaging from the Blanco Cosmology Survey and from pointed Magellan telescope observations, as well as spectroscopy using Magellan facilities, we confirm the existence of clustered red-sequence galaxies, report red-sequence photometric redshifts, present spectroscopic redshifts for a subsample, and derive R_{200} radii and M_{200} masses from optical richness. The clusters span redshifts from 0.15 to greater than 1, with a median redshift of 0.74; three clusters are estimated to be at $z > 1$. Redshifts inferred from mean red-sequence colors exhibit 2% RMS scatter in $\sigma_z/(1+z)$ with respect to the spectroscopic subsample for $z < 1$. We show that M_{200} cluster masses derived from optical richness correlate with masses derived from South Pole Telescope data and agree with previously derived scaling relations to within the uncertainties. Optical and infrared imaging is an efficient means of cluster identification and redshift estimation in large Sunyaev-Zel'dovich surveys, and exploiting the same data for richness measurements, as we have done, will be useful for constraining cluster masses and radii for large samples in cosmological analysis.

Subject headings: galaxies: clusters: individual, cosmology: observations

high@physics.harvard.edu
[1] Department of Physics, Harvard University, 17 Oxford Street, Cambridge, MA 02138
[2] Department of Astronomy, University of Illinois, 1002 West Green Street, Urbana, IL 61801
[3] Department of Physics and Astronomy, Cardiff University, CF24 3YB, UK
[4] University of Chicago, 5640 South Ellis Avenue, Chicago, IL 60637
[5] Fermi National Accelerator Laboratory, P.O. Box 500, Batavia, IL 60510
[6] National Center for Supercomputing Applications, University of Illinois, 1205 West Clark Street, Urbana, IL 61801
[7] Department of Physics & Astrophysics, University of North Dakota, Grand Forks, ND 58202
[8] Department of Physics, University of California, Berkeley, CA 94720
[9] Kavli Institute for Cosmological Physics, University of Chicago, 5640 South Ellis Avenue, Chicago, IL 60637
[10] Enrico Fermi Institute, University of Chicago, 5640 South Ellis Avenue, Chicago, IL 60637
[11] Institut dAstrophysique de Paris, 98bis bd Arago, F-75014 Paris, France
[12] Los Alamos National Laboratory, Los Alamos, New Mexico
[13] Department of Physics, University of Chicago, 5640 South Ellis Avenue, Chicago, IL 60637
[14] Harvard-Smithsonian Center for Astrophysics, 60 Garden Street, Cambridge, MA 02138
[15] Department of Astronomy and Astrophysics, University of Chicago, 5640 South Ellis Avenue, Chicago, IL 60637
[16] Department of Physics, McGill University, 3600 Rue University, Montreal, Quebec H3A 2T8, Canada
[17] Department of Astrophysical and Planetary Sciences and Department of Physics, University of Colorado, Boulder, CO 80309
[18] Departamento de Astronomia, Universidad de Chile, Casilla 36-D, Santiago, Chile
[19] University of California Observatories & Department of Astronomy, University of California, Santa Cruz, CA 95064
[20] Department of Space Science, VP62, NASA Marshall Space Flight Center, Huntsville, AL 35812
[21] Physics Division, Lawrence Berkeley National Laboratory, Berkeley, CA 94720
[22] (Institute for Physics and Mathematics of the Universe, University of Tokyo, 5-1-5 Kashiwa-no-ha, Kashiwa-shi, Chiba 277-8568, Japan
[23] Department of Physics, University of Michigan, 450 Church Street, Ann Arbor, MI, 48109
[24] Department of Physics, Ludwig-Maximilians-Universität, Scheinerstr. 1, 81679 München, Germany
[25] Excellence Cluster Universe, Boltzmannstr. 2, 85748 Garching, Germany
[26] Max-Planck-Institut für extraterrestrische Physik, Giessenbachstr. 85748 Garching, Germany
[27] Physics Department, Case Western Reserve University, Cleveland, OH 44106
[28] Department of Physics, Yale University, P.O. Box 208210, New Haven, CT 06520-8120
[29] Cerro Tololo Interamerican Observatory, La Serena, Chile
[30] University of Pittsburgh, 3941 O'Hara St., Pittsburgh, PA 15260

1. INTRODUCTION

Galaxy clusters are laboratories for both astrophysics and cosmology (Evrard 2004). Clusters represent the most massive dark matter halos, and their number density as a function of cosmic time is highly sensitive to dark energy (Wang & Steinhardt 1998; Haiman et al. 2001; Holder et al. 2001; Battye & Weller 2003; Molnar et al. 2004; Wang et al. 2004; Lima & Hu 2007). The mass of these systems is dominated by dark matter, but the primary means of observing clusters—especially large samples of them—are the luminous baryons of the hot intracluster gas and the galaxies themselves. The formation of the halos is well understood, while the precise behavior of the baryons is not as well modeled (see Voit 2005, for a review). This gap must be closed so that data from large cluster surveys can place precise constraints on cosmological parameters over a wide range of redshifts. Multi-wavelength observations of a cleanly selected, redshift-independent sample of galaxy clusters are a potentially powerful method of achieving this.

Searches for galaxy clusters using the Sunyaev-Zel'dovich (SZ) effect (Sunyaev & Zel'dovich 1972) promise to provide such a clean, redshift-independent sample. The SZ effect is scattering of cosmic microwave background photons to higher energy by the hot electrons in galaxy clusters (Birkinshaw 1999). The SZ surface brightness is independent of redshift but is closely related to cluster mass and so it is expected to be an excellent method for creating approximately mass-limited samples extending over a wide redshift range (Carlstrom et al. 2002). The constraints on cosmological parameters from such samples are complementary to geometrical tests using type Ia supernovae and baryon acoustic oscillations (e.g., Vikhlinin et al. 2009). Two SZ surveys, the Atacama Cosmology Telescope (ACT; Fowler et al. 2007) and the South Pole Telescope (SPT; Carlstrom et al. 2009) projects, are well positioned to provide large surveys which can be used for growth of structure studies.

Staniszewski et al. (2009, hereafter S09) presented the first discovery of previous unknown galaxy clusters using their SZ signature. Cluster redshifts are needed in addition to SZ data to provide the strongest constraints on dark energy. Coordinated optical follow-up observations can provide the needed redshift measurements. The Blanco Cosmology Survey (BCS; Ngeow et al. 2006, and `http://cosmology.illinois.edu/BCS/`), an NOAO survey program (2005-2008), provided multiband optical observations for the initial follow-up of portions of the first SPT survey fields. These data were used to identify optical counterparts to the S09 sample, search for giant arcs, explore possible cluster superpositions, and derive photometric redshifts.

Cluster mass can be estimated using several methods: the SZ and X-ray luminosity, which are sensitive to intracluster electrons; the number, luminosity, and velocity dispersion of cluster galaxies; and from gravitational lensing, which is the most direct probe of total cluster mass. Menanteau & Hughes (2009) characterized the galaxy counts and luminosity of the S09 cluster sample, and McInnes et al. (2009) subsequently explored their weak gravitational lensing signals.

Using data acquired by the SPT in 2008, Vanderlinde et al. (2010, hereafter V10) present an additional 17 SZ-detected clusters. Here we describe coordinated optical imaging of the catalog of 21 uniformly selected SZ detections, and new spectroscopic results on 8 of the clusters. Counterparts to a subset have been found in the catalogs of Abell et al. (1989, hereafter A89) and Menanteau et al. (2010, hereafter SCS-II). Seven clusters fell within the BCS footprint. For the remaining 14 clusters, and also for a subset of the BCS sample, we conducted pointed imaging observations and, for 8 clusters, spectroscopic observations, with the Magellan telescopes. The photometry was used to search for overdensities of red-sequence galaxies near the SZ locations, and if present, estimate their redshifts and also characterize their mass via optical red-sequence galaxy counts, or *richness*.

We describe in §2 the observations and data reduction. Section 3 outlines the redshift and richness analysis we used, and §4 describes the results on redshift (§4.1) and richness (§4.2). In Section 5 we discuss the results, and conclude with §6.

Throughout this paper we assume a flat concordance ΛCDM universe, with $(\Omega_\Lambda, \Omega_M, h) = (0.736, 0.264, 0.71)$ (Dunkley et al. 2009). All magnitudes are in the Sloan Digital Sky Survey (SDSS) *griz* AB system.

2. DATA ACQUISITION & REDUCTION

Cluster detection was achieved using millimeter-wavelength data from the South Pole Telescope, and optical imaging and spectroscopy provided cluster confirmation and redshift and richness estimates.

2.1. *South Pole Telescope*

The sample of 21 clusters presented here and in V10 is the first cosmologically significant catalog of clusters selected via the SZ effect. The sample was selected from two SPT survey fields totaling 178 deg^2 at R.A. = 23^h30^m, Decl. = $-55°$ and R.A. = 5^h30^m, Decl. = $-55°$ (J2000). Both fields were observed with arcminute resolution to an equivalent white noise level of 18 μK-arcmin[31].

The SPT time-ordered data were filtered and binned into maps, with the filtering acting roughly as a 1° high-pass filter in the R.A. direction. Clusters were extracted from these maps using a matched filter approach based on the work of (Haehnelt & Tegmark 1996; Herranz et al. 2002a,b; Melin et al. 2006). Spatial filters were constructed to maximize detection significance within a set of cluster profiles. The SPT astrometry is based on comparisons of radio source positions derived from SPT maps and positions of those sources in the AT20G catalog (Murphy et al. 2010), and should be accurate to 5″.

Cluster candidates were then identified by selecting all peaks above a fixed significance threshold and choosing the filter scale which produced the maximum detection significance ξ. A 3 parameter model for M_{200} involving ξ and the cluster redshift is presented in V10, along with the details of the SPT data reduction.

[31] The unit K refers to equivalent fluctuations in the CMB temperature, i.e., the level of temperature fluctuation of a 2.73 K blackbody that would be required to produce the same power fluctuation. See V10.

2.2. *Blanco Cosmology Survey*

BCS is an NOAO survey program to obtain deep *griz* imaging of two southern fields centered at R.A. = $23^{\rm h}00^{\rm m}$, Decl. = $-55°12'$ and R.A. = $5^{\rm h}30^{\rm m}$, Decl. = $-52°47'$ (J2000), each roughly 50 $\deg^2$. The 2008 SPT survey fields are larger than the BCS fields and include the entire BCS regions. BCS was conducted from 2005–2008 using the Mosaic-II wide-field imager on the Blanco 4 m telescope at Cerro Tololo Inter-American Observatory. Mosaic-II is an array of eight 2 k × 4 k CCDs with a pixel scale of $0.270''$ pixel^{-1} and a 0.36 $\deg^2$ field of view. The strategy was to obtain deep, contiguous *griz* imaging of the survey fields. In addition, BCS imaging was carried out for 7 photometric redshift calibration fields which include a sample of several thousand published spectroscopic redshifts.

The BCS data were processed and calibrated using a data management system developed for the Dark Energy Survey (Ngeow et al. 2006; Mohr et al. 2008) and run on the NCSA TeraGrid IA-64 Linux cluster. Data reduction includes crosstalk correction, overscan correction, bias subtraction, flat fielding, fringe and illumination corrections, field distortion correction, standard star photometric calibration, coadd-stacking, and photometric extraction of sources. BCS stacks typically reach 5σ galaxy photometry limits of 24.75, 24.65, 24.35 and 23.5 mag in *griz*, corresponding, for example, to a $0.5L^*$ cluster elliptical at $z = 1$. Completeness measurements in a typical field that are derived from comparison with deeper, better seeing CFHT data suggest 50% completeness limits of 24.25, 24.0, 23.75 and 23.0 in *griz* (Zenteno et al. in prep.).

2.3. *Magellan*

2.3.1. *Imaging*

For clusters that fell outside the BCS coverage region, for 5 that were within the BCS region, and for the unconfirmed candidate (see §4.3) we obtained *griz* imaging with the Inamori Magellan Areal Camera and Spectrograph (IMACS; Dressler et al. 2003; Osip et al. 2008) and Low Dispersion Survey Spectrograph (LDSS3; see Osip et al. 2008)—both in imaging mode—on the twin Magellan 6.5 m telescopes. IMACS is on the Magellan Baade telescope at the $f/11$ Nasmyth focus. Its circular field of view in $f/2$ mode subtends 0.20 $\deg^2$, mapped onto a 8192×8192 pixel, 8-chip CCD array, for a pixel scale of $0.200''$ pixel^{-1}. LDSS3 is on the Magellan Clay telescope at the $f/11$ Nasmyth focus, and its roughly 60 arcmin^2 circular field of view maps onto a subregion of a 4064×4064 pixel CCD, at a pixel scale of $0.189''$ pixel^{-1}.

Using the science-tested pipeline described by Rest et al. (2005) and Miknaitis et al. (2007), the same image reduction operations described above were performed on the Magellan images. Instead of using standard stars for photometric calibration, however, we employ Stellar Locus Regression (SLR; High et al. 2009) using stars that appear in the cluster images themselves. SLR delivers photometric calibrations by regressing the instrumental color-color locus of stars in any field to the known, astrophysically fundamental locus in the AB system. SLR enabled us to forego observations of standard stars altogether, maximizing the total integration time on the cluster fields.

The principal difference in strategy between Magellan and BCS observations is that the Magellan exposure times were adaptive rather than uniform. We first exposed for roughly 100 s in *griz*, searched for a cluster in the images, and continued with additional exposures if none was found. In median seeing of $0.8''$, these exposures reach nominal, 5σ point-source limiting magnitudes of 24.8, 24.8, 24.4, and 23.4 mag in *griz*. If no cluster was detected with the initial set of images, we acquired further exposures until a detection was achieved at a depth of approximately 1 to $0.4L^*$ with respect to the early-type cluster galaxies. This strategy results in highly variable depth for the Magellan imaging, but is the most efficient use of telescope time for follow-up observations.

Combined optical and SZ images are shown in Appendix A, Figures 7–28.

2.3.2. *Spectroscopy*

Spectroscopic data were acquired with LDSS3 in long-slit mode for the purpose of measuring redshifts. Given limited telescope time for spectroscopy, we observed only a subset of the confirmed clusters. The subset was chosen to span the widest possible range in redshifts, so that we could assess the performance of our red-sequence redshift measurement methodology (see §3.2 and §4.1).

We obtained low-resolution spectra of galaxies in the field of 8 SPT clusters, using the VPH-Red and VPH-All grisms. The median seeing was about $0.7''$ and conditions were photometric. Standard CCD processing and 2D-spectrum extraction, with preliminary wavelength solutions, were accomplished with the COSMOS reduction package[32]; the 1D spectra were then extracted using the APALL task in IRAF. We employed our own IDL routines to flux calibrate the data and remove telluric absorption using the well-exposed continua of the spectrophotometric standards (Wade & Horne 1988; Foley et al. 2003).

3. ANALYSIS

We adopted a standard red-sequence model for optical cluster detection, photometric redshifts, and richness estimation. As previously introduced, spectroscopic data on about half the clusters were used to empirically correct the red-sequence model colors and then verify photometric red-sequence redshifts over a long redshift baseline.

3.1. *Red-Sequence Model*

Red-sequence models were derived from the work of Bruzual & Charlot (2003), reflecting passively evolving, instantaneous-burst stellar populations with a formation redshift of $z = 3$, using Bertelli et al. (1994) evolutionary tracks and the Chabrier (2003) initial mass function. At each redshift, a range of metallicities was chosen by including a randomization in the metallicity-luminosity relation. The models were smoothed by linear fits in color-magnitude space at each redshift, and finally interpolated to arbitrary redshift using cubic splines.

[32] http://obs.carnegiescience.edu/Code/cosmos/

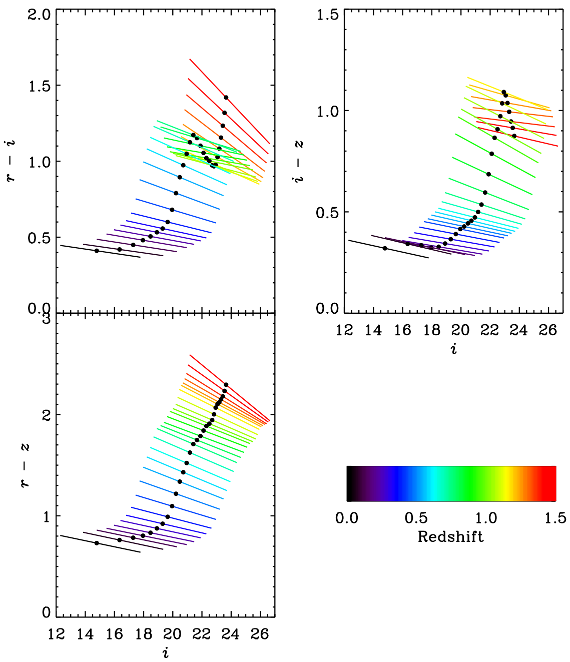

Fig. 1.— Red-sequence color-magnitude models as a function of redshift. Galaxy colors $r - i$ and $i - z$ were fit simultaneously in the red-sequence analysis, because that particular combination of colors (namely, $r-z = (r-i)+(i-z)$) allows for monotonic mapping from color to redshift over the widest redshift range ($0 < z \lesssim 1.4$) using optical wavelengths. The apparent i band magnitude of M^* at each redshift is denoted with the black points.

We made an empirical correction to the model using the subsample of 10 clusters with spectroscopic data. After performing the red sequence peak finding (§3.2), we plotted red sequence redshifts against spectroscopic redshifts. The best fit line through the data was measured to have slope 0.89 ± 0.03 and y-intercept 0.04 ± 0.02. Model colors were then corrected by reassigning the model redshifts to be equal to the inverse of this linear relation. The effect of the model color correction is to leave redshifts near the pivot, $z \sim 0.4$, roughly unchanged, and to boost redshifts near ~ 1 by about $\Delta z = +0.07$, or $\Delta z = +3.5\%(1 + z)$. The resulting red-sequence model is shown in Figure 1.

3.2. *Red-Sequence Finding and Redshifts*

We confirm the existence of clusters by searching near the SZ cluster coordinate for a background-subtracted excess of red-sequence objects, effectively segregated by redshift. At each redshift step of size $\Delta z = 0.01$ in the range $0.1 < z < 1.4$, and with an aperture of $2'$ radius around the SZ coordinate, we select all objects with a photometric signal-to-noise ratio > 5 in riz, whose $r - i$ and $i - z$ colors are also within 2σ of the red-sequence model line. The total uncertainty, e.g., for $r-i$, is defined as

$$\sigma^2 \equiv \sigma_{ri}^2 + \sigma_{ri}^{\mathrm{rs}\,2}, \tag{1}$$

and likewise for $i - z$. Here σ_{ri} (σ_{iz}) is the photometric uncertainty in $r - i$ ($i - z$) color of an object, and $\sigma_{ri}^{\mathrm{rs}}$ ($\sigma_{iz}^{\mathrm{rs}}$) is the intrinsic color scatter of the red sequence. These colors were chosen because their combination, $r - z = (r - i) + (i - z)$, increases monotonically over a long baseline of redshift, $0 < z \lesssim 1.4$. We assume $(\sigma_{ri}^{\mathrm{rs}}, \sigma_{iz}^{\mathrm{rs}}) = (0.05, 0.05)$ mag (Koester et al. 2007; Menci et al. 2008; Mei et al. 2009). The intrinsic scatter in color of cluster ellipticals alone is about two times smaller than this, and has been shown to be constant with redshift out to $z \approx 1.2$ (Menci et al. 2008; Mei et al. 2009). Morphological and spectral galaxy classification is beyond the scope of this work, and we assume our red sequence selections contain S0 galaxies in addition to ellipticals. This increases the color scatter and may also effectively induce redshift evolution due to evolving S0 populations; we ignore the latter effect, as the small number of clusters presented here is not sufficient to constrain redshift evolution.

We sum the selected galaxies, and normalize the counts by the projected area. This yields total surface density of all objects with colors consistent with the red-sequence model, within the $2'$ aperture, as a function of redshift, $\Sigma_{\mathrm{total}}(z)$. Uncertainties are estimated as the square root of counts, divided by the area.

The background red-sequence surface density is measured in a similar way. In the same set of riz exposures, we count red-sequence objects within many adjacent apertures of size $5' \times 5'$ over the entire field of view, excluding the $2'$ region around the SPT candidate position. The background surface density at each redshift, $\Sigma_{\mathrm{background}}(z)$, is calculated as the median of area-normalized counts from all apertures, and the uncertainty is the standard deviation divided by the square root of the total number of apertures. This approach is meant to minimize the contamination of the background signal by the red galaxies in the clusters themselves.

The red-sequence excess as a function of redshift is

$$\Sigma_{\mathrm{net}} = \Sigma_{\mathrm{total}} - \Sigma_{\mathrm{background}} \tag{2}$$

in units of galaxies per arcmin^2. We then renormalize the red sequence excess Σ_{net} in each redshift bin such that each galaxy contributes a *constant area* under the curve. The reason for this is that one galaxy may fall into multiple adjacent bins due to the size of color uncertainties, sometimes significantly widening the red-sequence peaks, especially for faint objects. The renormalization is a measure to mitigate this effect.

A cluster is detected if (1) there is an excess of red galaxies of the same apparent color in false color images, and (2) the galaxies corresponding to the maximum overdensity, $\Sigma_{\mathrm{net}}(z_{\mathrm{max}})$, are those identifiable in the false-color images. The cluster photometric redshift is taken to be z_{max}. Figure 2 illustrates the process of red-sequence finding for one of the SZ clusters.

3.2.1. *Completeness*

We tested for completeness in red-sequence finding at representative BCS and Magellan depths. After constructing mock optical catalogs (Song et al. in prep.) containing simulated clusters of mass above $\sim 3 \times 10^{14}\,h^{-1}\,M_{\odot}$, we searched for red-sequence overdensities as we have described. Our estimated completeness is the fraction of clusters recovered from the mock catalog. These mock catalogs include clusters with red and blue galaxy populations that are tuned to match the populations observed in real clusters (e.g., Lin et al. 2004). The galaxy distribution in space is determined using subhalo positions within high-resolution N-body simulations, and so the mock cluster spatial, kinematic and

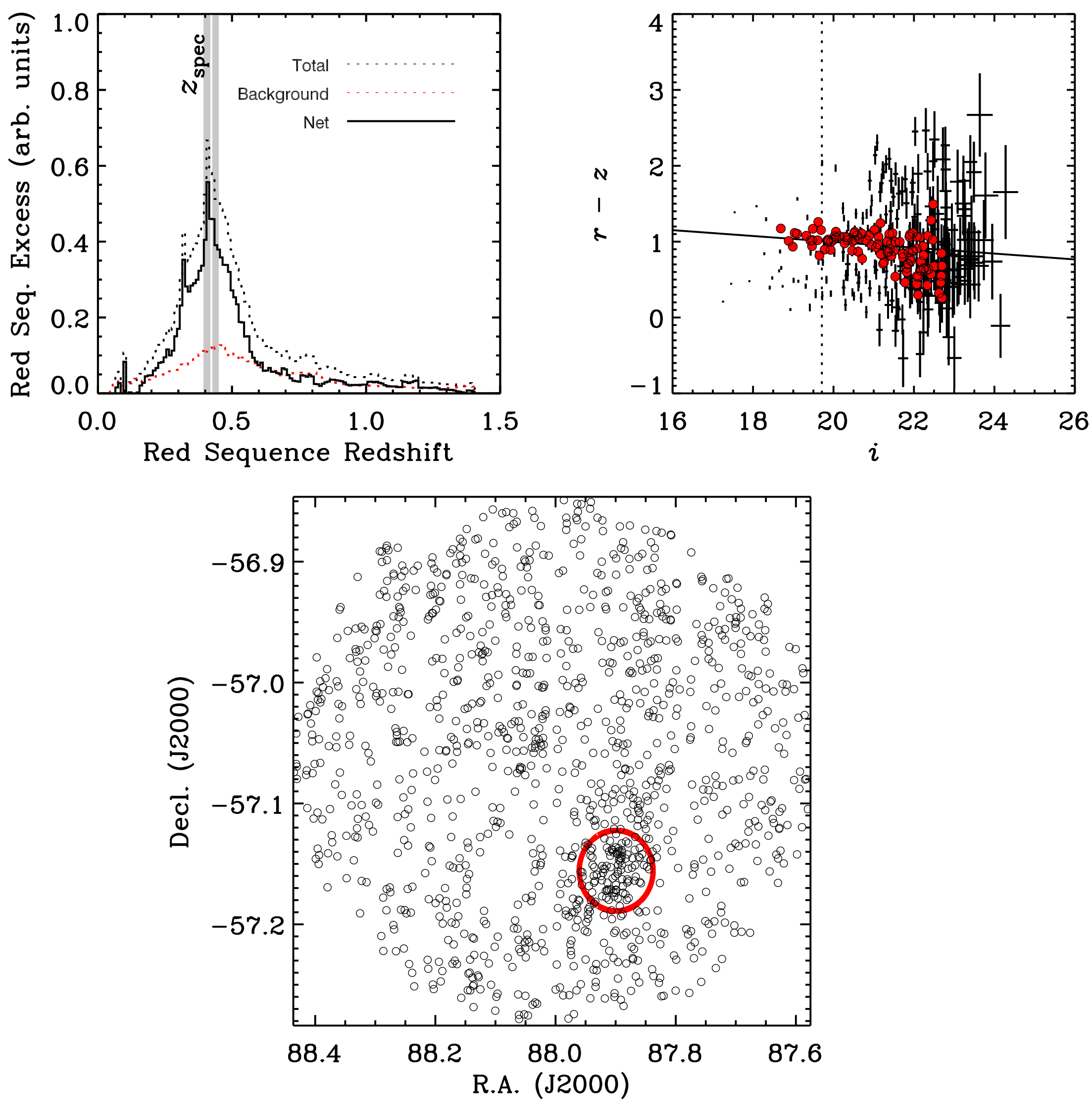

FIG. 2.— An illustration of red-sequence finding for the cluster SPT-CL J0551-5709 at $z_{\rm spec} = 0.4230$. The top left plot shows the surface density of objects consistent within 2σ of the red-sequence model as a function of redshift. The peak occurs at redshift $z_{\rm max} = 0.41$, which is consistent with the spectroscopic redshift (vertical white line, with $\sigma_z = 2\%(1+z)$ uncertainty region shaded in gray for illustration). The color-magnitude diagram for all objects within $2'$ of the SPT coordinate is shown in the upper right, and the subsample of red-sequence objects at $z_{\rm max}$ shown as red points. The vertical dotted line is the model m^* at this redshift. Positions of all objects consistent with the $z_{\rm max}$ red sequence are shown in the bottom panel, where we have also circled the cluster aperture. A spatial overdensity of objects is clearly seen at the aperture.

color signatures are a good match to those seen in real clusters.

The resulting selection function is shown in Figure 3. We recovered 100% of simulated clusters above the given mass threshold up to redshift 0.9. At this point the 4000 Å break begins to redshift out of the i band, making galaxies much harder to detect in $i-z$ color space. The completeness begins to fall here, and for these BCS and Magellan depths the probability of finding an optical counterpart above this mass threshold falls to zero by $z \approx 1.2$. Near-infrared photometry or much deeper space based optical photometry is required to push reliably to higher redshifts. But for the current sample only a single SPT cluster candidate was not confirmed using this multiband optical method.

3.3. $N_{\rm gal}$ and N_{200} Richness

After confirming a cluster and estimating its redshift, we measured the optical richness using a procedure that emulates the MaxBCG richness estimator (Koester et al. 2007), but adapted to high-redshift clusters. This began by again selecting objects with color within 2σ of the red-sequence line at redshift $z_{\rm max}$; luminosity brighter than $0.4L^*$ and fainter than the brightest cluster galaxy (BCG); and position within a projected radius of $R = 1\,h^{-1}$ Mpc of the cluster center. We binned the selected objects in i band magnitude bins of size $\Delta m = 0.4$. We subtracted the background, as before, by performing the same procedure in many apertures on the sky away from the cluster but in the same exposures, and normalizing by projected area. The background was subtracted from

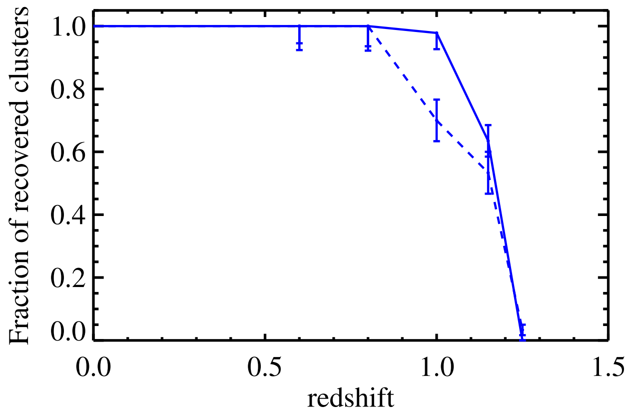

Fig. 3.— This shows the completeness of optical cluster finding from tests on a mock galaxy catalog with depth representative of the BCS survey (solid line) and Magellan imaging (dashed line). We have approximated Magellan data here as having limiting magnitudes ~ 1 magnitude brighter than BCS.

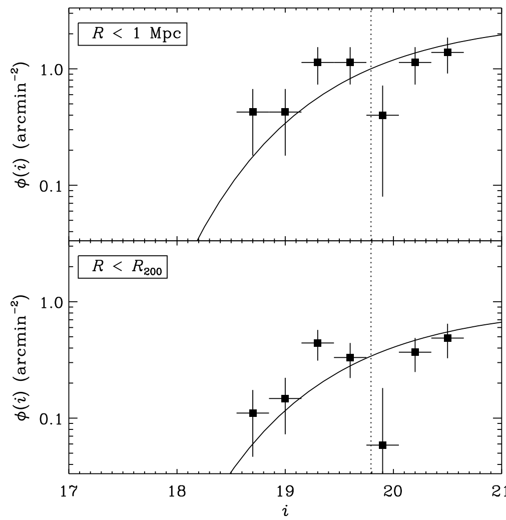

Fig. 4.— An illustration of luminosity function fitting for SPT-CL J0551-5709. We use our passively evolving model to fix m^* to 19.77 mag (vertical dotted line), and integrate down to $m^* + 1$ to estimate $N_{\rm gal}$ (top panel) and N_{200} (bottom panel). R_{200} is estimated from $N_{\rm gal}$, as described in the text.

the total red-sequence counts in each magnitude bin.

We then fitted Schechter luminosity functions (LF, Schechter 1976) to the i band magnitudes of the selected objects:

$$\phi(m){\rm d}m = 0.4\ln(10)\phi^* 10^{-0.4(m-m^*)(\alpha+1)} \times \exp\left[-10^{-0.4(m-m^*)}\right]{\rm d}m, \quad (3)$$

where m^* is the characteristic magnitude of the LF, α is the faint-end slope, and ϕ^* is the normalization. Our photometry was not uniformly complete on all clusters with respect to m^*, so our ability to constrain the slope was weak. We therefore fixed $\alpha = -1$, which has been shown to be reasonable for the most massive MaxBCG clusters (Lin & Mohr 2003; Hansen et al. 2005; Rudnick et al. 2009; Crawford et al. 2009). We tested fixing m^* at each redshift using our passive model, and leaving it free. For those clusters for which the luminosity function was well constrained, we measured values consistent with the model, and we ultimately chose to fix this parameter at each redshift. This is in agreement with the detailed LF studies of Zenteno et al. (in prep) on a subset of these clusters. The faint-end slope α has been shown to evolve with redshift (Rudnick et al. 2009), however, such studies must be performed at magnitudes fainter than m^*+1. We test varying α by ± 0.3, and find our richness results are largely unaffected to within our uncertainties. Because we integrate only to $m^* + 1$ there is only weak sensitivity to the adopted faint-end slope.

We fit the LF only at magnitudes brighter than our limiting magnitude and fainter than the BCG. Limiting magnitudes are estimated to be the faintest magnitude bin before which the red-sequence background becomes incomplete, as indicated by a deviation from linearity in the logarithmic i band magnitude distribution of red-sequence galaxies. We also assess photometric completeness using simulated point sources in our cluster images. We determine that we recover 90% of simulated objects in images at *all magnitudes* brighter than the above-defined limiting magnitude. The majority of unrecovered objects are lost to pixel masking due to bright stars and to object crowding. We make a generic correction by this amount in all magnitude bins, the effect of which is to increase $N_{\rm gal}$ estimates by 0.9^{-1}. The analytic LF is then integrated down to $m^* + 1$. The resulting integration is an estimate of $N_{\rm gal}$, which is the number of red sequence galaxies within $1\,h^{-1}$ Mpc of the cluster center, above a fixed luminosity threshold.

We stress that the LF fitting step deviates from the MaxBCG procedure, but it is necessary because our photometry is not complete to $0.4L^*$ on all clusters. Our fitting and extrapolating the LF of fairly bright, red-sequence satellite galaxies is physically reasonable because it is known that the luminosity function of such members of massive clusters is only very weakly dependent on mass and is well described by a Schechter function from lower redshifts (Hansen et al. 2009) to redshifts close to unity (Gilbank et al. 2008). Figure 4 illustrates the resulting LF fit for one of the SPT clusters.

R_{200} is estimated from $N_{\rm gal}$ using the empirical $N_{\rm gal}$–R_{200} relation of Hansen et al. (2005),

$$R_{200} = 0.156 N_{\rm gal}^{0.6}\,h^{-1}\,{\rm Mpc}. \quad (4)$$

This relation was measured from the MaxBCG cluster sample, which ranged in redshift from 0.1 to 0.3 and had a median mass of about $1 \times 10^{14}\,h^{-1}\,M_\odot$. The clusters we present in this work are mostly above this redshift range, and expected to have higher median mass (see V10, §4.2). Nonetheless, we adopt this relation to estimate cluster radii, and leave verification of the relation on an SZ selected sample such as this to future work.

The entire richness procedure is repeated, now setting $R = R_{200}$ instead of $1\,h^{-1}$ Mpc, to arrive at an estimate of N_{200}. N_{200} is then used to estimate cluster mass using previously established empirical relations, which we now outline.

3.3.1. *Mass-Richness Scaling and Scatter*

By comparing to weak gravitational lensing masses, N_{200} richness has been shown by Reyes et al. (2008)

to scale with M_{200}, the cluster mass contained within a sphere that has an average mass density of 200 times the universal average, as

$$\frac{M_{200}}{10^{14}h^{-1}\,M_\odot} = (1.42 \pm 0.08)\left(\frac{N_{200}}{20}\right)^{1.16\pm0.09}. \quad (5)$$

Earlier, Johnston et al. (2007) presented a similar, independent weak lensing study, and their relation (normalization 0.88 ± 0.12, power law 1.28 ± 0.04) differs from Equation (5) by about 30% in mass at $5 \times 10^{14}\,h^{-1}\,M_\odot$. We adopt Equation (5) as our mass-richness scaling relation with overall uncertainty of 30%.

Scatter in M_{200} at fixed $N_{200} = 40$ as determined from weak lensing and X-ray cluster masses is $\sigma_{M|N} = 45\% \pm 20\%$ (95% CL, Rozo et al. 2009).

If richness quantities scale as

$$M_{200} \sim N_{200}^{1/\alpha} \sim N_{\rm gal}^{1/(\alpha\beta)} = N_{\rm gal}^{1/0.56} \sim R_{200}^3, \quad (6)$$

where α is the N_{200}–M_{200} power law and β is the $N_{\rm gal}$–N_{200} power law, then $\alpha = 0.86$ and $\beta = 0.65$, using results of Equations (4) and (5). Scatter of 45% (60%) in mass translates to scatter of 39% (52%) in N_{200}, 25% (34%) in $N_{\rm gal}$, and 15% (20%) in R_{200}.

As with the $N_{\rm gal}$–R_{200} relation (Equation (4)), these N_{200}–M_{200} mass relations were determined from weak lensing measurements of MaxBCG clusters in SDSS, a sample that was deemed to be complete at redshifts $0.1 < z < 0.3$, with median mass of approximately $1 \times 10^{14}\,h^{-1}\,M_\odot$. Our SZ selected cluster sample has a significantly broader redshift distribution, as well as a median mass about five times larger. Red galaxies are known to be biased tracers of dark matter, and the bias is a function of mass, redshift, and radius. Given the small size of our sample and the large intrinsic uncertainties inherent to richness techniques, we assume our data are insensitive to deviations from these fiducial relations, and we leave the study of the evolution of red galaxy populations with larger SZ cluster samples to future work.

3.3.2. *Statistical Richness Uncertainties*

We estimated statistical uncertainties on $N_{\rm gal}$ and N_{200} by bootstrapping (Efron 1979) the entire richness procedure thousands of times. In particular, we assumed that the statistically limiting step in our procedure was the luminosity function fitting to the binned magnitude data. Therefore, the start of the bootstrap process was a random resampling of the magnitude bins themselves. For each realization, we re-fitted the luminosity function, integrated to obtain $N_{\rm gal}$, and estimated R_{200}. We independently bootstrapped the LF fitting for N_{200} estimation as well. Parameters were assigned as the biweight means (Beers et al. 1990) of bootstrap distributions, and sample uncertainties as the biweight standard deviations.

3.4. *Spectroscopic Redshifts*

For each galaxy spectrum, the redshift was found by cross-correlating with the FABTEMP97 template, using the RVSAO package in IRAF (Kurtz & Mink 1998). The validity of the cross-correlation redshift was checked by visual inspection and judged by the presence of visible absorption (and in a few cases, emission) lines. Redshift uncertainties were estimated as two times those given by RVSAO for the BCG redshifts, or the biweight interval estimator (Beers et al. 1990) for the other cases. We discard non-galactic spectra as well as redshifts in strong disagreement with the ensemble average or our prior photometric redshift estimate. The redshift adopted for each cluster is the median redshift of the galaxies passing all cuts.

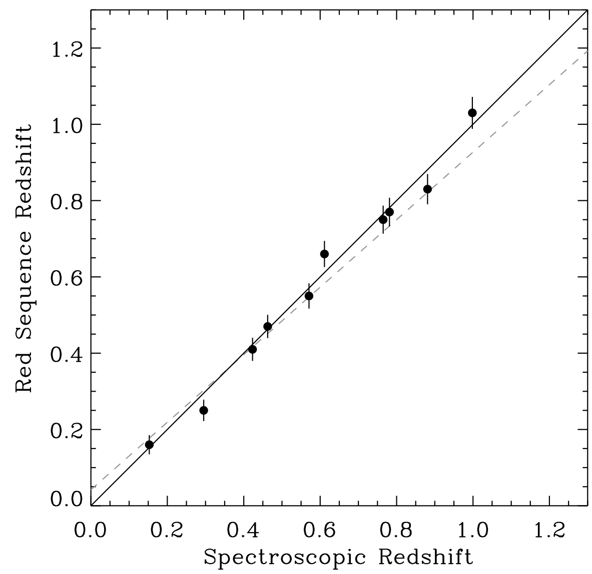

Fig. 5.— Spectroscopic versus red-sequence redshifts. We have applied an empirical linear correction to the red-sequence model colors using this sample, and this plot shows the result of red-sequence redshift measurements after the model correction. The best fit line to the uncorrected redshifts is the dashed line, shown for comparison. Typical RMS redshift scatter is about 2% in $\sigma_z/(1+z)$. Redshift estimates for the entire sample are presented in Table 1.

4. RESULTS

4.1. *Redshifts*

We list redshift results in Table 1. Figure 5 is a plot of red sequence redshifts versus spectroscopic redshifts for clusters on which we have both measurements. The line we fitted to uncorrected redshifts, which were used to empirically calibrate the red-sequence model colors (§3.1), is the dashed line in the figure. After the correction, we verify that the red sequence redshifts are unbiased to within the uncertainties. Root-mean-square scatter in redshift per cluster is $\sigma_z = 0.02(1 + z)$, with maximum absolute deviation of $0.05(1 + z)$. We therefore generically assign random uncertainties of 2% to all redshifts in the range we have directly tested, $0.15 < z < 1$. For redshifts estimated to be > 1, we assign 5% uncertainties in order to effectively rule out redshifts less than 1. Finally, for clusters at $z < 1$ where our photometric uncertainties are large, we also generically increase the uncertainty estimates.

4.2. *Richness*

In Figure 6 we compare our richness-derived masses to those presented in V10, which were estimated from

TABLE 1
CLUSTER REDSHIFT DATA

Cluster Name	z_{rs}	z_{spec}	N_{spec}	Imaging Coverage BCS?	Imaging Coverage Magellan?
SPT-CL J0509-5342	0.47(3)	0.4626(4)	6	Y	Y
SPT-CL J0511-5154	0.74(3)	···	···	N	Y
SPT-CL J0516-5430	0.25(3)	0.2952	8	Y	Y
SPT-CL J0521-5104	0.72(3)	···	···	Y	N
SPT-CL J0528-5259	0.75(4)	0.7648(5)	2	Y	Y
SPT-CL J0533-5005	0.83(4)	0.8810(9)	4	N	Y
SPT-CL J0539-5744	0.77(4)	···	···	N	Y
SPT-CL J0546-5345	1.16(11)	···	···	Y	N
SPT-CL J0551-5709	0.41(3)	0.4230(10)	5	N	Y
SPT-CL J0559-5249	0.66(3)	0.6112(3)	5	N	Y
SPT-CL J2259-5617	0.16(2)	0.1528	1	N	Y
SPT-CL J2300-5331	0.29(3)	···	···	N	Y
SPT-CL J2301-5546	0.78(9)	···	···	N	Y
SPT-CL J2331-5051	0.55(3)	0.5707(5)	8	N	Y
SPT-CL J2332-5358	0.32(3)	···	···	Y	Y
SPT-CL J2337-5942	0.77(4)	0.7814(5)	2	N	Y
SPT-CL J2341-5119	1.03(4)	0.9983(5)	1	N	Y
SPT-CL J2342-5411	1.08(10)	···	···	Y	N
SPT-CL J2332-5521	···	···	···	Y	Y
SPT-CL J2355-5056	0.35(3)	···	···	N	Y
SPT-CL J2359-5009	0.76(4)	···	···	N	Y
SPT-CL J0000-5748	0.74(9)	···	···	N	Y

NOTE. — See §4.3 for notes on individual clusters, including those which have been identified in other works.

SPT millimeter-wavelength data. We label V10 masses as $M(\xi)$, because they are calculated from the SZ signal-to-noise ratio ξ. The purpose of the comparison is to assess the level of correlation and explore whether the power law and normalization of the scaling laws are consistent with previous work. We additionally estimate the normalization of N_{gal}, which we treat as an empirical mass observable in its own right rather than only as a measurement intermediate to N_{200}.

Richness and $M(\xi)$ are plotted against one another in Figure 6. We have used Equation (5) to render the far right-hand mass axis, with the 30% overall uncertainty in this relation denoted with the heavy error bar. We do not display a mass axis in the N_{gal} panel of the figure because there have been no previous measurements of an N_{gal}–M_{200} scaling relation.

We perform the analysis only considering clusters whose radius (R_{200} in the case of N_{200}, $1\,h^{-1}$ Mpc in the case of N_{gal}) falls fully within the observed field of view. For Magellan IMACS imaging this limited radii to $\lesssim 6'$, because we placed the SPT center in the middle of one of the eight chips, at a distance of about six arcminutes from the field edge. Spatial incompleteness of this kind does not affect the BCS data.

4.2.1. N_{gal} *Scaling*

R_{200} for massive clusters is approximately $1.5\,h^{-1}$ Mpc, which subtends $\gtrsim 6'$ at redshifts $z \lesssim 0.3$. We find it useful to count red galaxy overdensities in a smaller region, corresponding to $1\,h^{-1}$ Mpc in co-moving coordinates, which subtends $\gtrsim 6'$ at redshifts $z \lesssim 0.17$. This is a better match to the observed typical angular size of the SZ signal. In addition, the surface density of red galaxies in the smaller aperture is greater than for R_{200}, whose larger area effectively dilutes the signal. For these reasons we explore N_{gal} as an empirical mass proxy.

As argued in § 3.3.1, N_{gal} should scale with mass as $M_{200}^{0.56}$. We fix this slope and measure

$$N_{gal} = (52 \pm 3 \pm 9)\left(\frac{M_{200}}{5 \times 10^{14}\,h^{-1}\,M_\odot}\right)^{0.56}, \quad (7)$$

If zero intrinsic scatter is assumed, the reduced chi-square of the fit is $\chi^2_\nu \approx 3$, whereas 20% in N_{gal} (corresponding to $\sim$ 35% in mass) produces $\chi^2_\nu = 1$. The first error given in Equation (7) is random-only, which includes the intrinsic mass-richness scatter, and the second error is the overall systematic uncertainty of 30%. This fit is shown as the solid black line in the left-hand panel of Figure 6.

Letting the slope be free, we measure a normalization consistent with Equation (7) and slope 0.42 ± 0.50. This is the dashed line in the left-hand panel of Figure 6. In the figure, the inner, dark shaded area denotes the 68% confidence region for the best two-parameter fit assuming zero intrinsic scatter, while the outer, light shaded area is the 68% confidence region for best two-parameter fit assuming 35% intrinsic mass scatter, which is a significantly better match to the data. We estimate the uncertainty on intrinsic scatter by varying it until the chi-square doubles, resulting in relative 1σ uncertainty at the $\sim$ 50% level.

4.2.2. N_{200} *Scaling*

We perform the same analysis on N_{200}. Fixing the mass-mass slope to unity, we measure

$$N_{200} = (57 \pm 4 \pm 15)\left(\frac{M_{200}}{5 \times 10^{14}\,h^{-1}\,M_\odot}\right)^{0.86}. \quad (8)$$

Again, 35% intrinsic mass scatter, corresponding to 30% scatter in N_{200}, gives $\chi^2_\nu = 1$. This fit is shown as the black line in right-hand panel of Figure 6, and can be compared to the one-to-one mass line, in red.

Letting the slope be free, the measured normalization consistent with Equation (8) and slope 0.62 ± 0.73. This

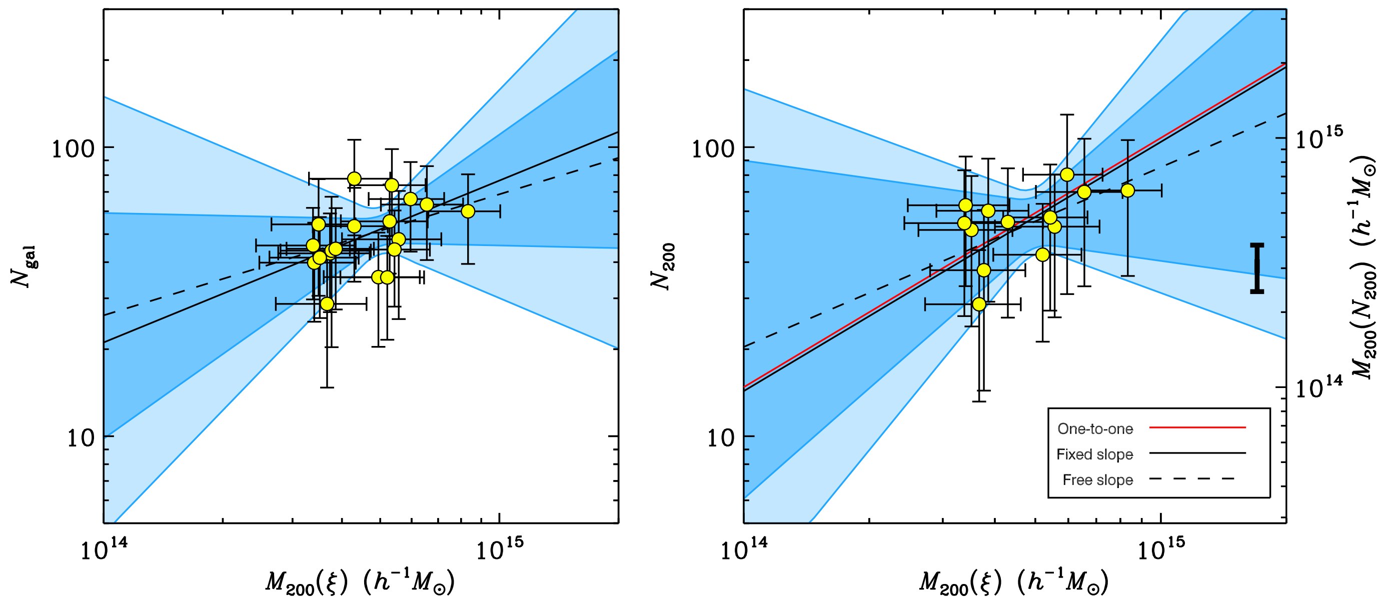

Fig. 6.— Optical richness versus total cluster mass estimated from the SPT data. This plot shows that the richness correlates highly with this millimeter-wavelength mass-observable (taken from Vanderlinde et al. 2010), and together the data agree with previously established scaling relations to within the uncertainties. The solid red line in the right-hand panel is the one-to-one mass relation, and the solid black lines in both panels are best-fit relations when fixing the slope to previously measured values. The dashed lines are best-fit relations leaving both slope and intercept free. The dark, inner shaded areas denote the 68% confidence regions assuming zero intrinsic richness-mass scatter for the two parameter regression. The light, outer shaded areas denote 68% confidence regions assuming 35% scatter in mass, which is a better match to the data. The heavy error bar on the far right-hand side indicates the nominal overall uncertainty of 30% in the N_{200}–M_{200} relation.

is shown with the dashed black line in Figure 6. As before, the dark, inner shaded region is the 68% confidence region for the best two-parameter fit assuming zero intrinsic scatter, while the outer, light shaded area is the 68% confidence region for best two-parameter fit assuming 35% intrinsic mass scatter, which is a significantly better match to the data. Relative uncertainty on the intrinsic scatter is comparable to that quoted above for $N_{\rm gal}$.

All richness results are given in Table 2. In the table we have adopted Equation (5) to estimate masses from N_{200}, and for $N_{\rm gal}$ masses we have used Equation (7). Systematic uncertainties are taken to be the quadrature sum of the nominal 45% intrinsic scatter in mass (§3.3.1) and the 30% overall uncertainty in the richness–mass scaling relation. Further work on a larger sample of clusters selected with similar criteria as these is needed to reduce statistical uncertainties and measure the scatter directly. We discuss the implications of our richness measurements in §5.

4.3. *Notable Clusters*

In this section we describe notable information, if any, about the clusters. As we will point out, a subset of clusters also appear in the catalogs of A89, Böhringer et al. (2004), S09, Menanteau & Hughes (2009, hereafter MH09), Menanteau et al. (2009, hereafter M09), and Menanteau et al. (2010, hereafter M10). Our redshifts agree to within $\sigma_z \approx 3\%(1+z)$ of the photometric redshifts presented in M09 and M10, except for the highest redshift cluster from S09, SPT-CL J0546-5345 (see below). Because we have not presented exhaustive optical cluster-finding in the entire BCS survey in this work, instead having concentrated on fields in the direction of the SZ detections, and because the number of overlapping clusters is too small to draw useful conclusions with high statistical confidence, we leave a formal inter-comparison of redshift and richness results of M09 and M10 to future studies.

SPT-CL J0509-5342— This cluster was previously identified by S09.

SPT-CL J0511-5154— This cluster has recently been identified by M10, who assigned the name SCSO J051145-515430.

SPT-CL J0516-5430— This cluster was previously identified by S09, where it was called by a different name, SPT-CL J0517-5430. The SPT name ascribed to this object in this work and in V10 follow the recommendations of the International Astronomical Union (IAU), and should be adopted permanently. This cluster also identified as Abell S0520 (Abell et al. 1989, hereafter A89), and RXCJ0516.6-5430 (Böhringer et al. 2004), the latter of which is the source of the spectroscopic redshift. M10 detected this object and call it SCSO J051637-543001.

SPT-CL J0521-5104— This cluster has been identified by M10 as SCSO J052113-510418.

SPT-CL J0528-5300— This cluster was previously identified by S09, where it was called by the same name, and was also identified by M10 as SCSO J052803-525945.

SPT-CL J0539-5744— This cluster displays a possible strong gravitational lens arc.

SPT-CL J0546-5345— This cluster was previously identified by S09, where it was called by a different name, SPT-CL J0547-5345. The SPT name ascribed to this object in this work and in V10 follow the recommendations of the IAU, and should be adopted permanently.

TABLE 2
Cluster Richness Data

Object Name	$N_{\rm gal}$[a]	$M_{200}(N_{\rm gal})$[b] $(10^{14}h^{-1}M_\odot)$	R_{200}[a] $(h^{-1}{\rm Mpc})$	N_{200}[a]	$M_{200}(N_{200})$[b] $(10^{14}h^{-1}M_\odot)$
SPT-CL J0509-5342	41(8)	$3.3 \pm 2.0 \pm 1.0$	1.46(17)	51(13)	$4.3 \pm 2.5 \pm 1.3$
SPT-CL J0511-5154	77(12)	$10.3 \pm 5.9 \pm 3.1$	2.13(20)	···	···
SPT-CL J0516-5430	···	···	···	···	···
SPT-CL J0521-5104	44(7)	$3.7 \pm 2.2 \pm 1.1$	1.52(15)	57(13)	$4.8 \pm 2.7 \pm 1.4$
SPT-CL J0528-5300	44(9)	$3.8 \pm 2.3 \pm 1.1$	1.52(18)	60(13)	$5.1 \pm 2.8 \pm 1.5$
SPT-CL J0533-5005	28(10)	$1.7 \pm 1.4 \pm 0.5$	1.17(25)	28(6)	$2.2 \pm 1.2 \pm 0.6$
SPT-CL J0539-5744	63(9)	$7.1 \pm 4.0 \pm 2.1$	1.88(16)	69(14)	$6.1 \pm 3.3 \pm 1.8$
SPT-CL J0546-5345	66(7)	$7.7 \pm 4.1 \pm 2.3$	1.93(12)	80(31)	$7.1 \pm 4.8 \pm 2.1$
SPT-CL J0551-5709	54(15)	$5.4 \pm 3.8 \pm 1.6$	1.71(29)	···	···
SPT-CL J0559-5249	59(6)	$6.5 \pm 3.4 \pm 1.9$	1.82(11)	70(8)	$6.2 \pm 3.2 \pm 1.8$
SPT-CL J2259-5617	···	···	···	···	···
SPT-CL J2300-5331	35(10)	$2.5 \pm 1.8 \pm 0.8$	1.33(22)	···	···
SPT-CL J2301-5546	35(8)	$2.5 \pm 1.6 \pm 0.8$	1.33(17)	42(6)	$3.4 \pm 1.8 \pm 1.0$
SPT-CL J2331-5051	73(5)	$9.4 \pm 4.8 \pm 2.8$	2.06(8)	···	···
SPT-CL J2332-5358	42(8)	$3.5 \pm 2.1 \pm 1.1$	1.49(16)	···	···
SPT-CL J2337-5942	53(8)	$5.2 \pm 2.9 \pm 1.6$	1.69(15)	55(11)	$4.6 \pm 2.5 \pm 1.4$
SPT-CL J2341-5119	39(7)	$3.1 \pm 1.9 \pm 0.9$	1.42(16)	62(7)	$5.4 \pm 2.8 \pm 1.6$
SPT-CL J2342-5411	43(19)	$3.7 \pm 3.4 \pm 1.1$	1.51(38)	37(12)	$2.9 \pm 1.8 \pm 0.9$
SPT-CL J2355-5056	55(5)	$5.6 \pm 3.0 \pm 1.7$	1.73(10)	···	···
SPT-CL J2359-5009	47(16)	$4.3 \pm 3.4 \pm 1.3$	1.59(32)	53(8)	$4.4 \pm 2.3 \pm 1.3$
SPT-CL J0000-5748	45(6)	$4.0 \pm 2.2 \pm 1.2$	1.55(12)	54(11)	$4.6 \pm 2.5 \pm 1.4$

Note. —
[a] Uncertainties given are statistical only.
[b] Uncertainties given are statistical and systematic, respectively.

S09 reported a photometric redshift of ~ 0.9 and M09 independently reported $z_{\rm photo} = 0.88^{+0.08}_{-0.04}$. We do not detect a red-sequence overdensity near redshift 0.9, but a faint red-sequence peak is evident at $z_{\rm rs} \approx 1.15$.

SPT-CL J0551-5709— Abell S0552 (A89) is in the foreground of this cluster. No redshift estimate exists for Abell S0552, but a strong red sequence at $z_{\rm rs} = 0.09$ is clearly visible in color-magnitude diagrams. The SPT cluster identified here, however, is measured at $z = 0.42$.

SPT-CL J0559-5249— Our red-sequence studies reveal two significant red galaxy overdensities, one at the redshift given in Table 1 and another at $z \approx 0.4$. On inspection of the spatial distribution of galaxies, we attribute the SZ signal to the higher redshift system.

SPT-CL J2259-5617— We identify this cluster with Abell 3950, and recover a spectroscopic redshift from archival data on what we identify as the BCG. The SPT SZ detection coordinate lies nearly exactly on the line joining the two Abell 3950 coordinates given in the literature, at a projected distance of 71″ from that quoted by Arp & Madore (1996), and 208″ from that quoted by A89. The redshift of Abell 3950 has not been previously measured, but we have identified the BCG in 2MASS as 2MASX J23000108-5617061, which the 6dF Galaxy Survey measured to be at $z_{\rm spec} = 0.152787$ (Jones et al. 2005). This galaxy lies 18″ from the SPT coordinate.

SPT-CL J2300-5331— We identify this with Abell S1079 (A89). No previous redshift estimates exist for this cluster.

SPT-CL J2331-5051— This cluster exhibits a giant gravitational lens arc and a well separated secondary cluster structure in both the optical and SZ data. This is among the most interesting of the clusters presented here, and is the subject of a dedicated study (High et al., in preparation).

SPT-CL J2332-5358— This cluster was recently identified by M10 as SCSO J233227-535827.

SPT-CL J2343-5521— No red-sequence cluster appears in BCS imaging, whose 50% completeness depth in the i band is 23.5 mag, corresponding to m^* at $z \approx 1.2$. Either there exists a cluster at higher redshift, or this is a false SZ detection. V10 show that the false detection rate is only 7% for clusters at equivalent SZ significance. However, the SZ profile radius is significantly larger than any other cluster, consistent with a cosmic microwave background fluctuation. Preliminary follow-up of this cluster at other wavelengths suggest this is indeed a false detection.

5. DISCUSSION OF SYSTEMATIC EFFECTS

The greatly different criteria with which our SZ clusters were selected as compared to the MaxBCG sample could give rise to differences in measured properties. One important effect is the evolution of the mean and scatter of red cluster-galaxy colors with redshift and mass. While elliptical (E) galaxies are highly homogeneous in the range of redshifts our sample represents, $0 < z \lesssim 1.2$ (Menci et al. 2008; Lidman et al. 2008; Mei et al. 2009), the mean and scatter of S0 galaxy colors are known to evolve with redshift and density of the environment (e.g., van Dokkum et al. 1998). The environment also causes color evolution with distance from the cluster center. Our method, and indeed that of MaxBCG, does not explicitly use morphological selection criteria, so we must assume E and S0 populations contribute to our richness estimates. Understanding color-selection effects at all redshifts for a large sample of clusters would require sophisticated simulations or full photometric redshift measurements that are beyond the scope of this work.

Another important effect is the evolution of the abundance of early-type cluster galaxies as a function of luminosity. Clusters have been observed to accumulate faint galaxies at a greater rate than bright ones over time, manifesting as evolution in the slope of the luminosity function's faint end, α, as a function of redshift (Rudnick et al. 2009). Despite our long redshift baseline, we expect our measurements here to be largely unaffected by behavior at the faint end, as we integrate the LF down to a relatively shallow magnitude of $m^* + 1$. Indeed, tests where we vary α have not significantly affected our results.

In addition, because our richness measurement is not exactly that used with maxBCG (from which the R_{200}–$N_{\rm gal}$ relationship that we use here is taken) our R_{200} estimates are likely to be somewhat overestimated (cf. discussion in Hansen et al. 2009). Using a larger-than-ideal aperture for counting red galaxies may contribute to some of the scatter in the richness-mass correlation that we observe here.

Red galaxy counting has nonetheless proven to be a simple and accessible way to estimate the total mass in clusters and groups. If this technique can be accurately extended to the very wide range of redshifts that SPT SZ-selected clusters span, then modeling and measuring evolutionary effects in SZ clusters will be useful to obtaining constraints on masses of very large cluster samples.

6. CONCLUSIONS

We have observed clusters from the 2008 South Pole Telescope SZ survey at optical and near-infrared wavelengths. We estimate redshifts and richness with red-sequence techniques, and we obtain spectroscopic redshifts for a subsample of the clusters.

Our red-sequence-derived redshifts exhibit 2% RMS scatter in $\sigma_z/(1+z)$ in the subsample with spectroscopic overlap, over the redshift range $0.15 < z < 1.0$. Our analysis provides no evidence that the SZ selected sample from SPT follows different scaling relations than those followed by SDSS optically selected clusters.

The clusters presented in this paper comprise the largest sample of galaxy clusters discovered with the SZ and demonstrates that current SZ surveys can detect many high-mass galaxy clusters across a wide range of redshifts. Precise dark energy constraints from these surveys require the cluster redshifts, masses, and selection function to be known. The SZ effect contains no redshift information, and coordinated observations at optical and infrared wavelengths are an efficient means of providing this, especially for large cluster samples. Optical cluster identification is also potentially useful for understanding SZ selection functions. In the future, there will probably be greater coverage of SZ clusters by OIR imaging than any other wavelength or observing method other than the millimeter-wavelength itself. Optical redshifts are essential for constraining cosmology with SZ surveys, and the same data may also be brought to bear on the mass and cluster selection problems.

This research has made use of the NASA/IPAC Extragalactic Database (NED) which is operated by the Jet Propulsion Laboratory, California Institute of Technology, under contract with the National Aeronautics and Space Administration. This publication has made use of data products from the Two Micron All Sky Survey, which is a joint project of the University of Massachusetts and the Infrared Processing and Analysis Center/California Institute of Technology, funded by the National Aeronautics and Space Administration and the National Science Foundation. This research has made use of the NASA/ IPAC Infrared Science Archive, which is operated by the Jet Propulsion Laboratory, California Institute of Technology, under contract with the National Aeronautics and Space Administration.

IRAF is the Image Reduction and Analysis Facility, distributed by the National Optical Astronomy Observatories, which are operated by the Association of Universities for Research in Astronomy, Inc., under cooperative agreement with the National Science Foundation.

We used the cosmology calculator tools of Wright (2006).

This work is supported by the NSF (AST-0607485, AST-0506752, ANT-0638937, ANT-0130612, MRI-0723073), the DOE (DE-FG02-08ER41569 and DE-AC02-05CH11231), NIST (70NANB8H8007), and Harvard University. B. Stalder and A. Loehr gratefully acknowledge support by the Brinson Foundation. R. J. Foley acknowledges the generous support of a Clay fellowship.

We also thank the team of scientists, engineers and observing staff of the Las Campanas Observatory and of Cerro Tololo Inter-American Observatory.

Facilities: Magellan:Baade (IMACS), Magellan:Clay

REFERENCES

Abell, G. O., Corwin, Jr., H. G., & Olowin, R. P. 1989, ApJS, 70, 1
Arp, H. C., & Madore, B. F. 1996, VizieR Online Data Catalog, 7170, 0
Battye, R. A., & Weller, J. 2003, Phys. Rev. D, 68, 083506
Beers, T. C., Flynn, K., & Gebhardt, K. 1990, AJ, 100, 32
Bertelli, G., Bressan, A., Chiosi, C., Fagotto, F., & Nasi, E. 1994, A&AS, 106, 275
Birkinshaw, M. 1999, Physics Reports, 310, 97
Böhringer, H., et al. 2004, A&A, 425, 367
Bruzual, G., & Charlot, S. 2003, MNRAS, 344, 1000
Carlstrom, J. E., et al. 2009, submitted to PASP, arXiv:0907.4445
Carlstrom, J. E., Holder, G. P., & Reese, E. D. 2002, ARA&A, 40, 643
Chabrier, G. 2003, PASP, 115, 763
Crawford, S. M., Bershady, M. A., & Hoessel, J. G. 2009, ApJ, 690, 1158
Dressler, A. M., Sutin, B. M., & Bigelow, B. C. 2003, in Society of Photo-Optical Instrumentation Engineers (SPIE) Conference Series, Vol. 4834, Society of Photo-Optical Instrumentation Engineers (SPIE) Conference Series, ed. P. Guhathakurta, 255–263
Dunkley, J., et al. 2009, ApJS, 180, 306
Efron, B. 1979, The Annals of Statistics, 7, 1
Evrard, A. E. 2004, 1
Foley, R. J., et al. 2003, PASP, 115, 1220
Fowler, J. W., et al. 2007, Appl. Opt., 46, 3444
Gilbank, D. G., Yee, H. K. C., Ellingson, E., Gladders, M. D., Loh, Y., Barrientos, L. F., & Barkhouse, W. A. 2008, ApJ, 673, 742
Haehnelt, M. G., & Tegmark, M. 1996, MNRAS, 279, 545+

Haiman, Z., Mohr, J. J., & Holder, G. P. 2001, ApJ, 553, 545
Hansen, S. M., McKay, T. A., Wechsler, R. H., Annis, J., Sheldon, E. S., & Kimball, A. 2005, ApJ, 633, 122
Hansen, S. M., Sheldon, E. S., Wechsler, R. H., & Koester, B. P. 2009, ApJ, 699, 1333
Herranz, D., Sanz, J. L., Barreiro, R. B., & Martínez-González, E. 2002a, ApJ, 580, 610
Herranz, D., Sanz, J. L., Hobson, M. P., Barreiro, R. B., Diego, J. M., Martínez-González, E., & Lasenby, A. N. 2002b, MNRAS, 336, 1057
High, F. W., Stubbs, C. W., Rest, A., Stalder, B., & Challis, P. 2009, AJ, 138, 110
Holder, G., Haiman, Z., & Mohr, J. J. 2001, ApJ, 560, L111
Johnston, D. E., et al. 2007, ArXiv e-prints, 0709.1159
Jones, D. H., Saunders, W., Read, M., & Colless, M. 2005, Publications of the Astronomical Society of Australia, 22, 277
Koester, B. P., et al. 2007, ApJ, 660, 221
Kurtz, M. J., & Mink, D. J. 1998, PASP, 110, 934
Lidman, C., et al. 2008, A&A, 489, 981
Lima, M., & Hu, W. 2007, Phys. Rev. D, 76, 123013
Lin, Y., & Mohr, J. J. 2003, ApJ, 582, 574
Lin, Y., Mohr, J. J., & Stanford, S. A. 2004, ApJ, 610, 745
McInnes, R. N., Menanteau, F., Heavens, A. F., Hughes, J. P., Jimenez, R., Massey, R., Simon, P., & Taylor, A. 2009, MNRAS, 399, L84
Mei, S., et al. 2009, ApJ, 690, 42
Melin, J.-B., Bartlett, J. G., & Delabrouille, J. 2006, A&A, 459, 341
Menanteau, F., & Hughes, J. P. 2009, ApJ, 694, L136
Menanteau, F., et al. 2010, ArXiv e-prints, 1002.2226
——. 2009, ApJ, 698, 1221
Menci, N., Rosati, P., Gobat, R., Strazzullo, V., Rettura, A., Mei, S., & Demarco, R. 2008, ApJ, 685, 863
Miknaitis, G., et al. 2007, ApJ, 666, 674
Mohr, J. J., et al. 2008, in Society of Photo-Optical Instrumentation Engineers (SPIE) Conference Series, Vol. 7016, Society of Photo-Optical Instrumentation Engineers (SPIE) Conference Series
Molnar, S. M., Haiman, Z., Birkinshaw, M., & Mushotzky, R. F. 2004, ApJ, 601, 22
Murphy, T., et al. 2010, MNRAS, 154
Ngeow, C., et al. 2006, in Society of Photo-Optical Instrumentation Engineers (SPIE) Conference Series, Vol. 6270, Society of Photo-Optical Instrumentation Engineers (SPIE) Conference Series
Osip, D. J., Floyd, D., & Covarrubias, R. 2008, in Society of Photo-Optical Instrumentation Engineers (SPIE) Conference Series, Vol. 7014, Society of Photo-Optical Instrumentation Engineers (SPIE) Conference Series
Rest, A., et al. 2005, ApJ, 634, 1103
Reyes, R., Mandelbaum, R., Hirata, C., Bahcall, N., & Seljak, U. 2008, MNRAS, 390, 1157
Rozo, E., et al. 2009, ApJ, 699, 768
Rudnick, G., et al. 2009, ApJ, 700, 1559
Schechter, P. 1976, ApJ, 203, 297
Staniszewski, Z., et al. 2009, ApJ, 701, 32
Sunyaev, R. A., & Zel'dovich, Y. B. 1972, Comments on Astrophysics and Space Physics, 4, 173
van Dokkum, P. G., Franx, M., Kelson, D. D., Illingworth, G. D., Fisher, D., & Fabricant, D. 1998, ApJ, 500, 714
Vanderlinde, K., et al. 2010, submitted to ApJ, arXiv:1003.0003
Vikhlinin, A., et al. 2009, ApJ, 692, 1060
Voit, G. M. 2005, Reviews of Modern Physics, 77, 207
Wade, R. A., & Horne, K. 1988, ApJ, 324, 411
Wang, L., & Steinhardt, P. J. 1998, ApJ, 508, 483
Wang, S., Khoury, J., Haiman, Z., & May, M. 2004, Phys. Rev. D, 70, 123008
Wright, E. L. 2006, PASP, 118, 1711

APPENDIX

GALLERY OF CLUSTERS

Figures 7–28 are false-color optical images of the clusters, together with the SZ detection significance maps. In all images, north is up, east is left.

The SZ-only insets subtend 8 arcminutes on a side. The mapping between color and SZ significance ξ is the same in all SZ thumbnails. The highest significance cluster, Figure 22, spans the largest color range, which is $\xi \in [-5.57, 14.94]$. The peak value in each thumbnail is equal to the quoted SZ detection significance in V10. Contours are given at steps of $\Delta(\xi) = 2$, and the corresponding values are labeled. Contours are dashed where ξ is negative, and solid where ξ is nonnegative.

The optical images have the same contours as their corresponding SZ thumbnail overlain, and subtend 1.5 Mpc in the cluster rest frame. We have mapped the zrg passbands to the RGB channels, respectively, so that the apparent redness of red-sequence cluster galaxies approximately increases with redshift.

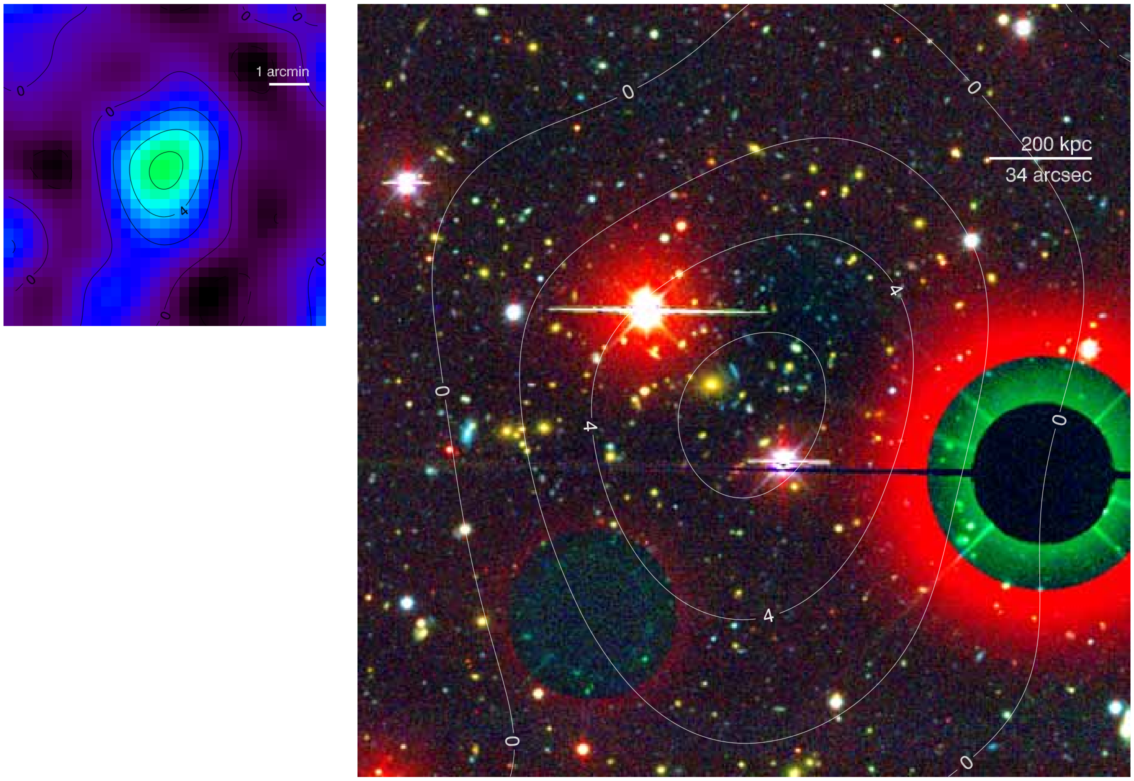

FIG. 7.— SPT-CL J0509-5342

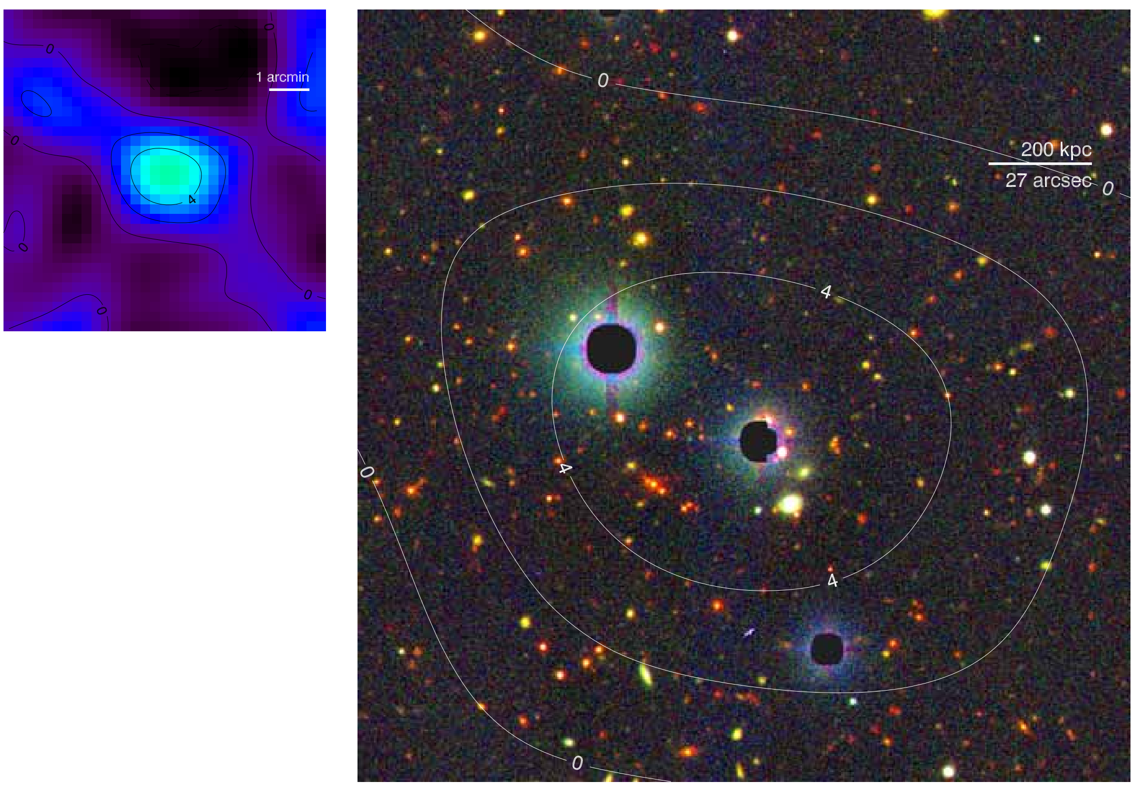

FIG. 8.— SPT-CL J0511-5154

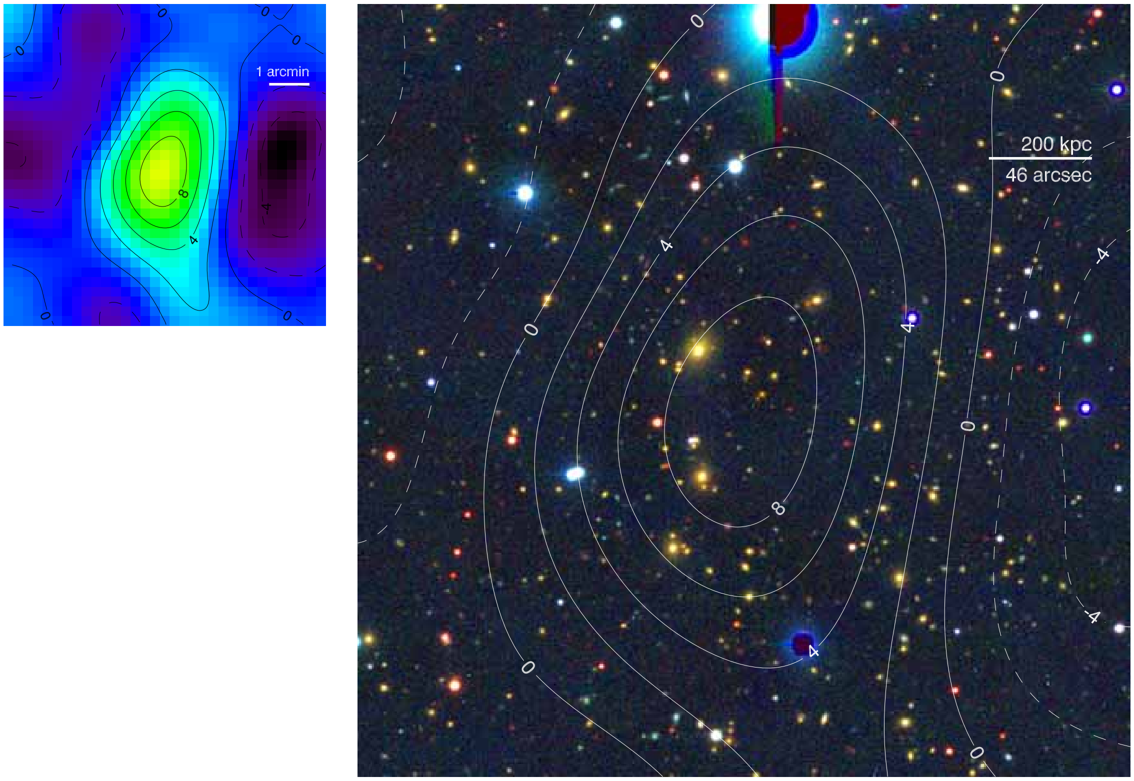

FIG. 9.— SPT-CL J0516-5430

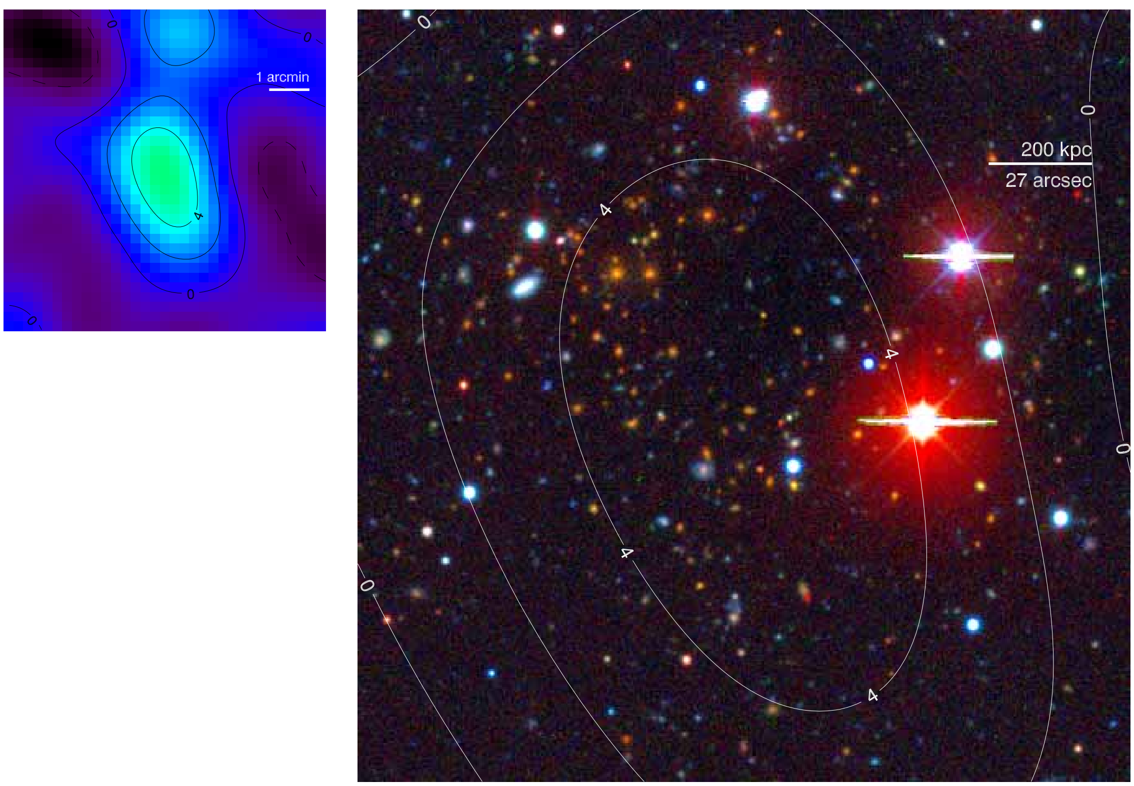

FIG. 10.— SPT-CL J0521-5104

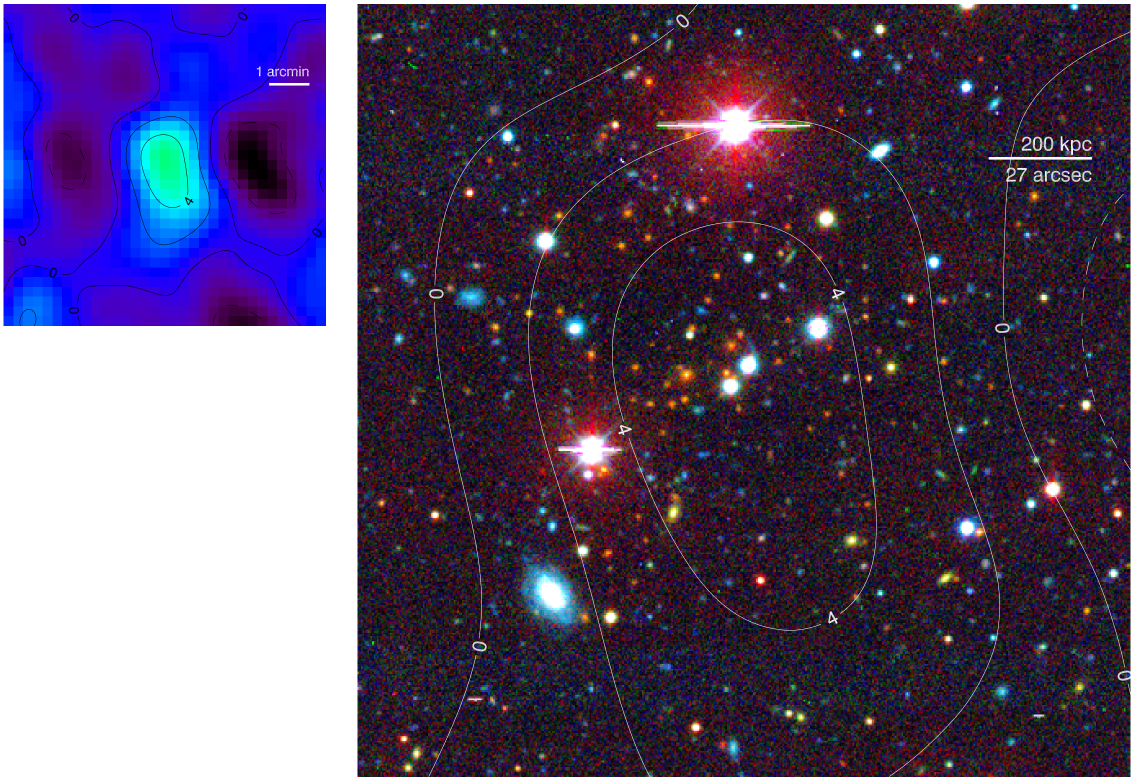

FIG. 11.— SPT-CL J0528-5300

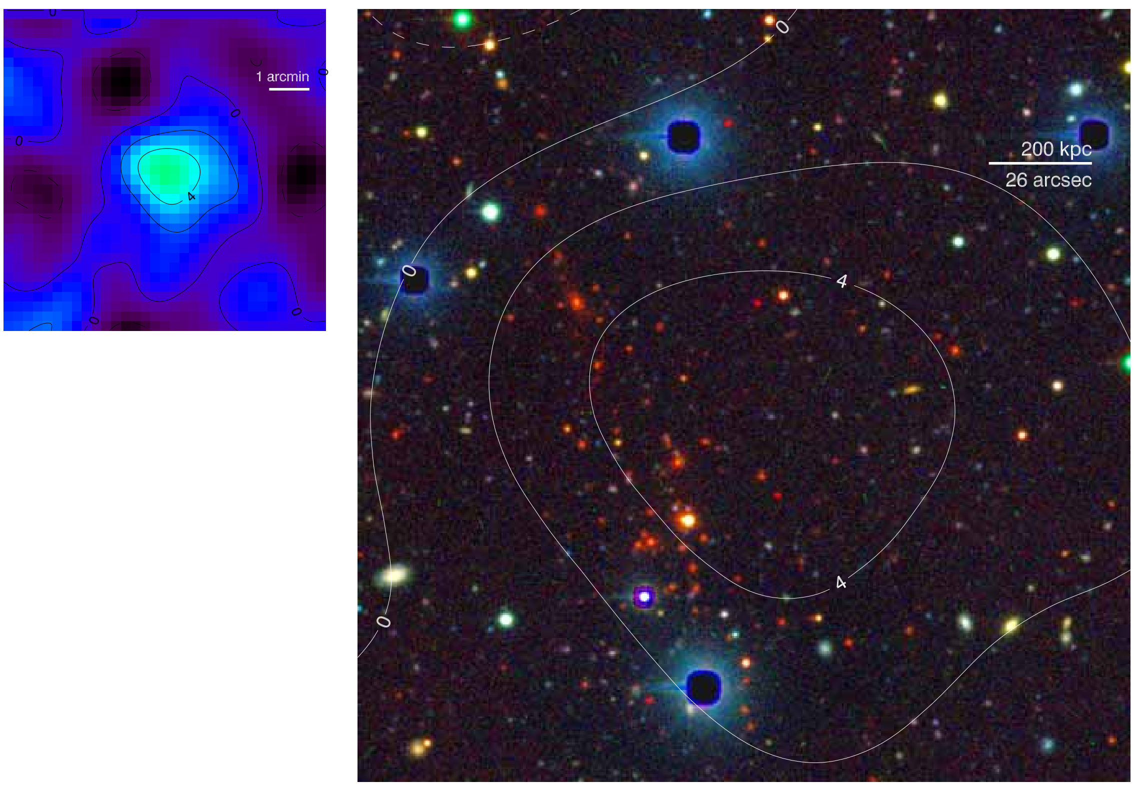

FIG. 12.— SPT-CL J0533-5005

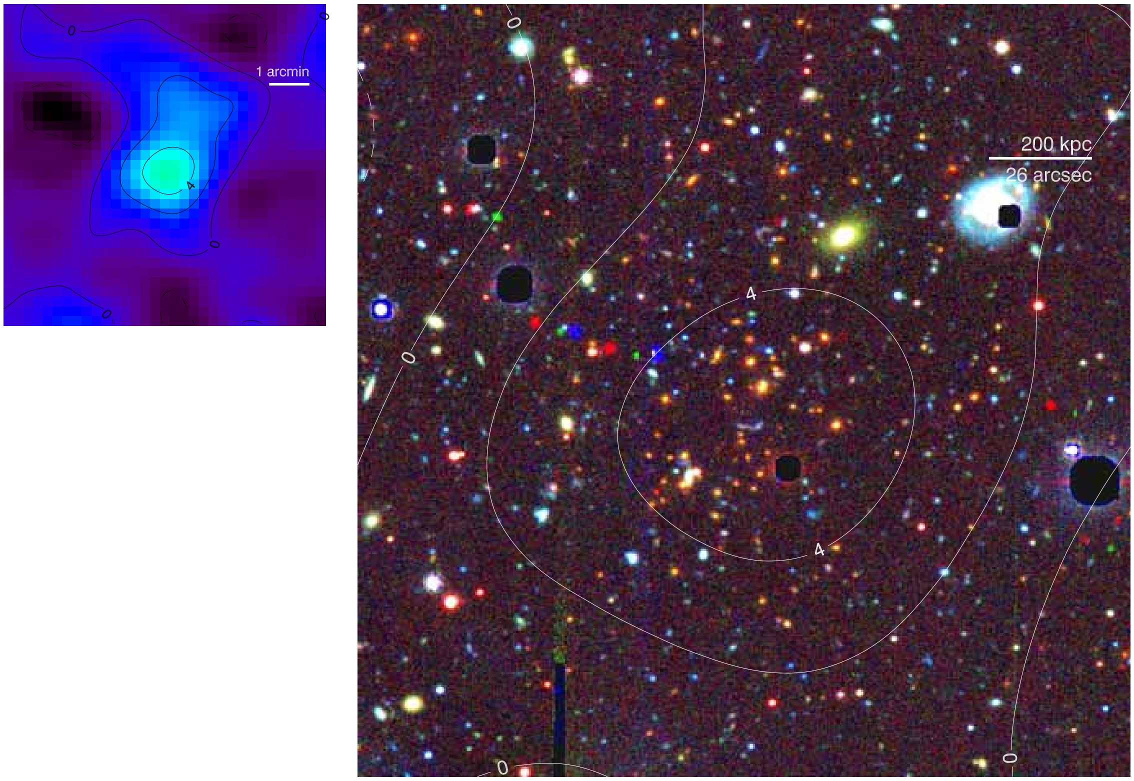

FIG. 13.— SPT-CL J0539-5744

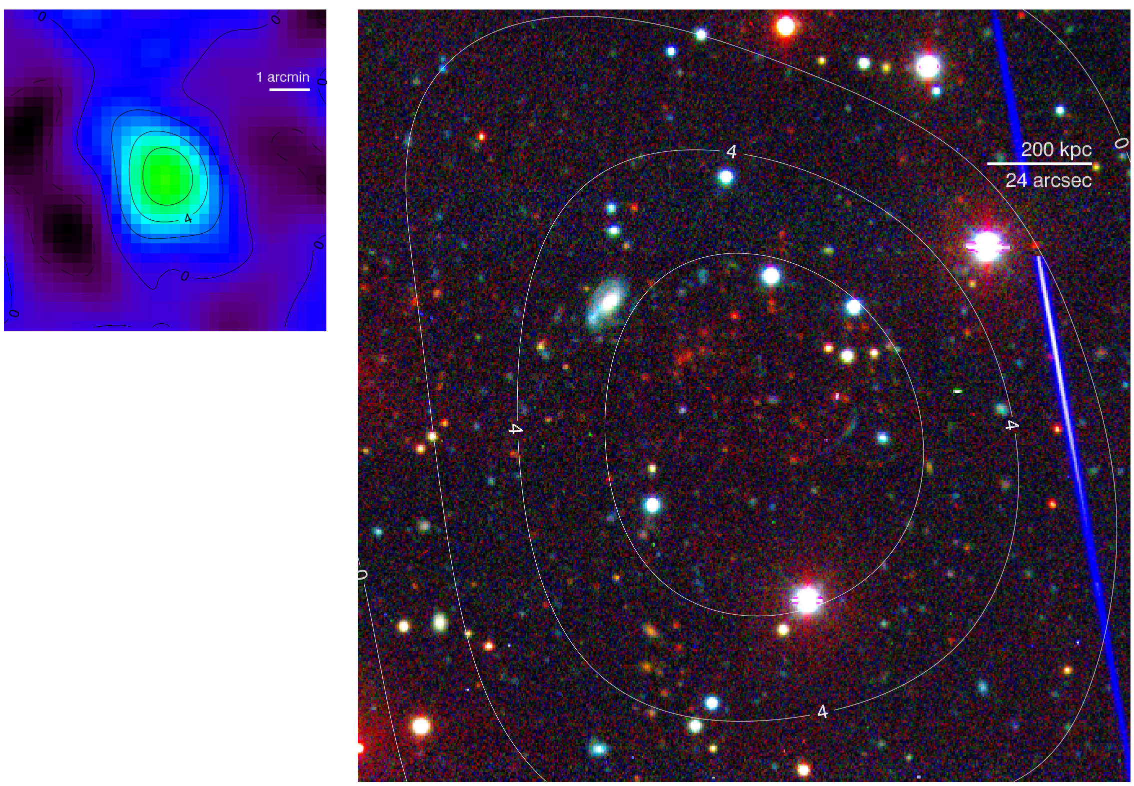

FIG. 14.— SPT-CL J0546-5345

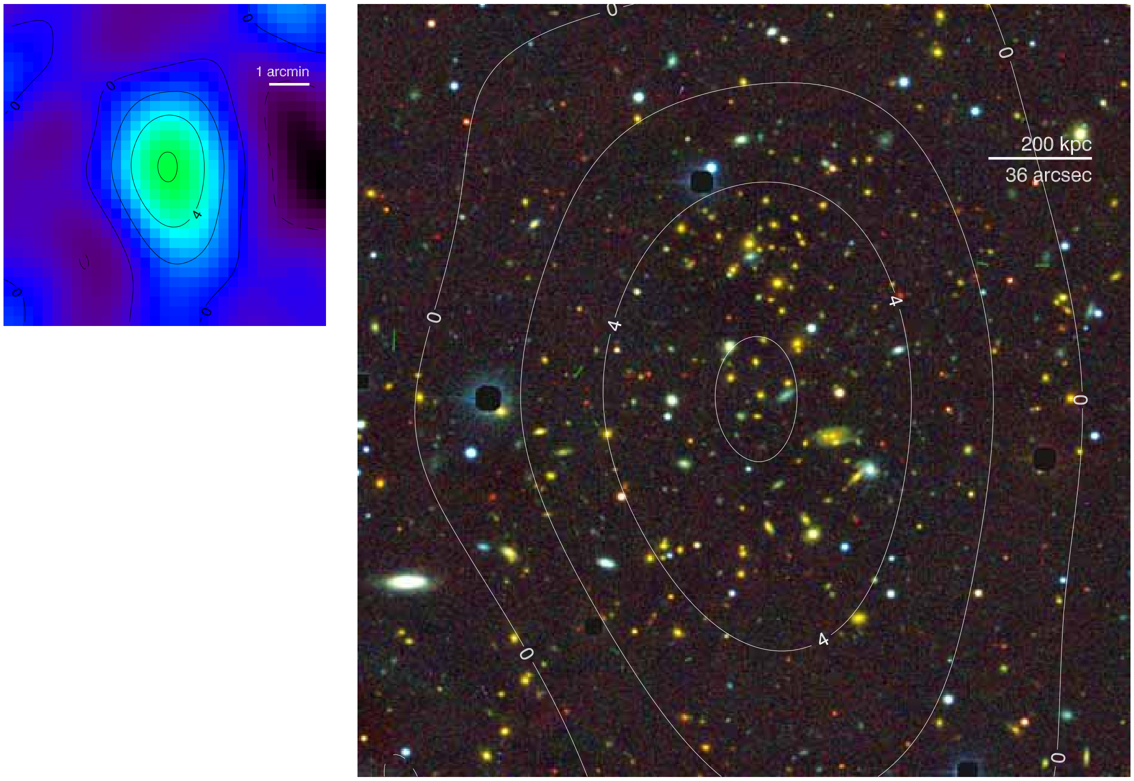

FIG. 15.— SPT-CL J0551-5709

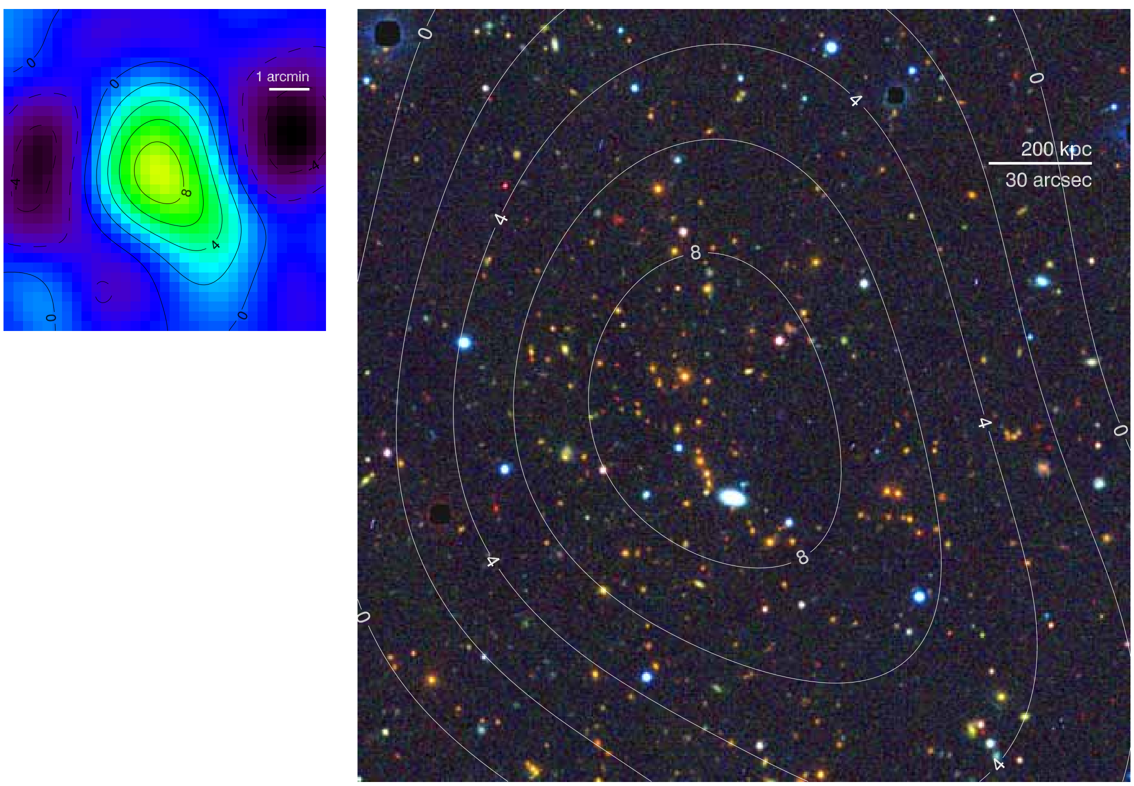

FIG. 16.— SPT-CL J0559-5249

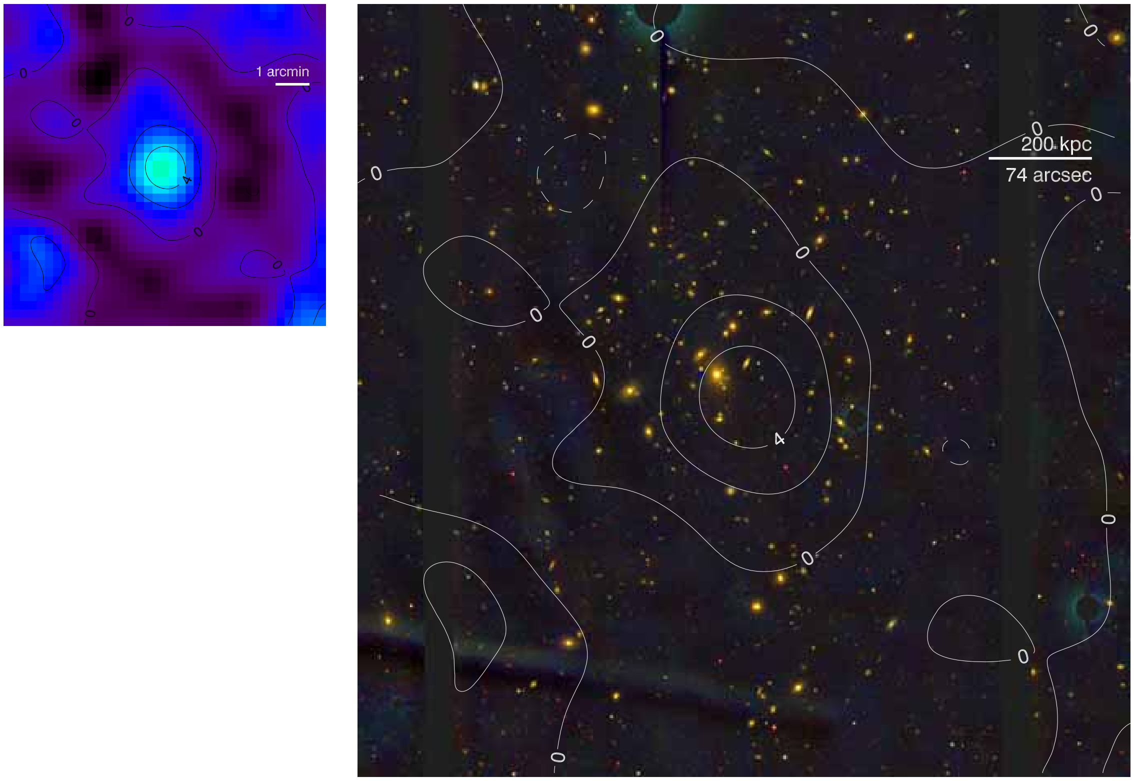

FIG. 17.— SPT-CL J2259-5617

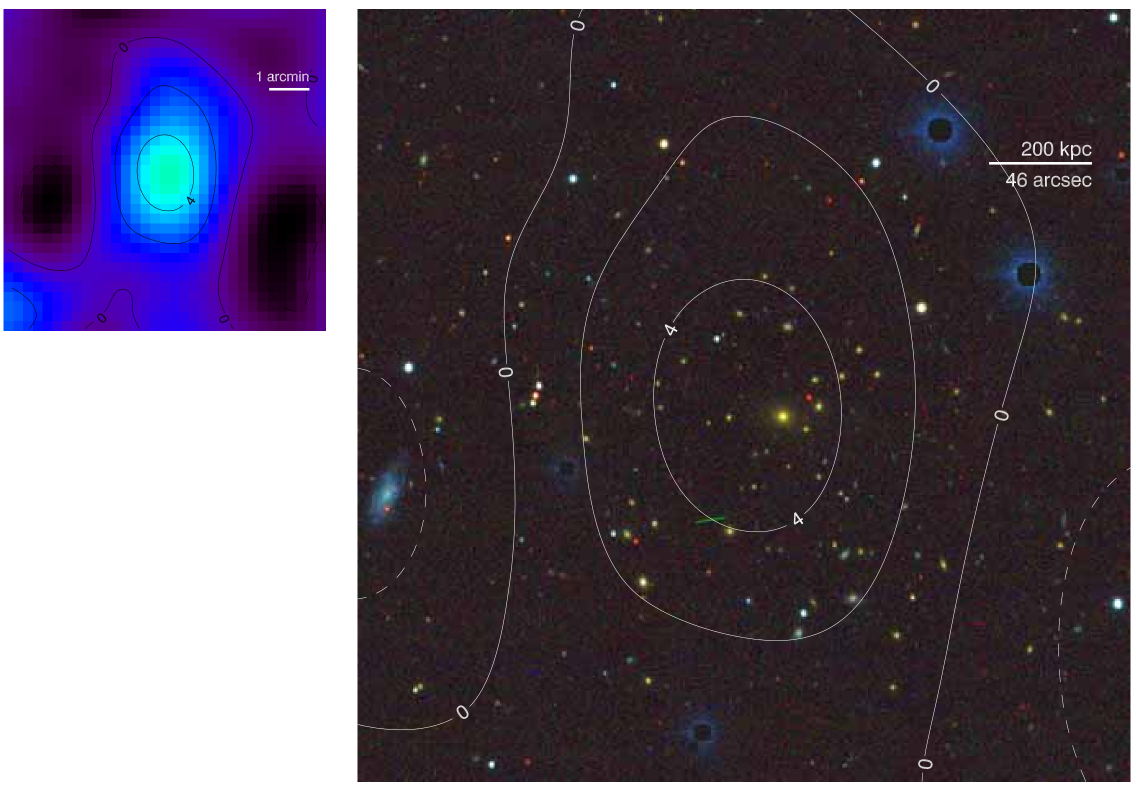

FIG. 18.— SPT-CL J2300-5331

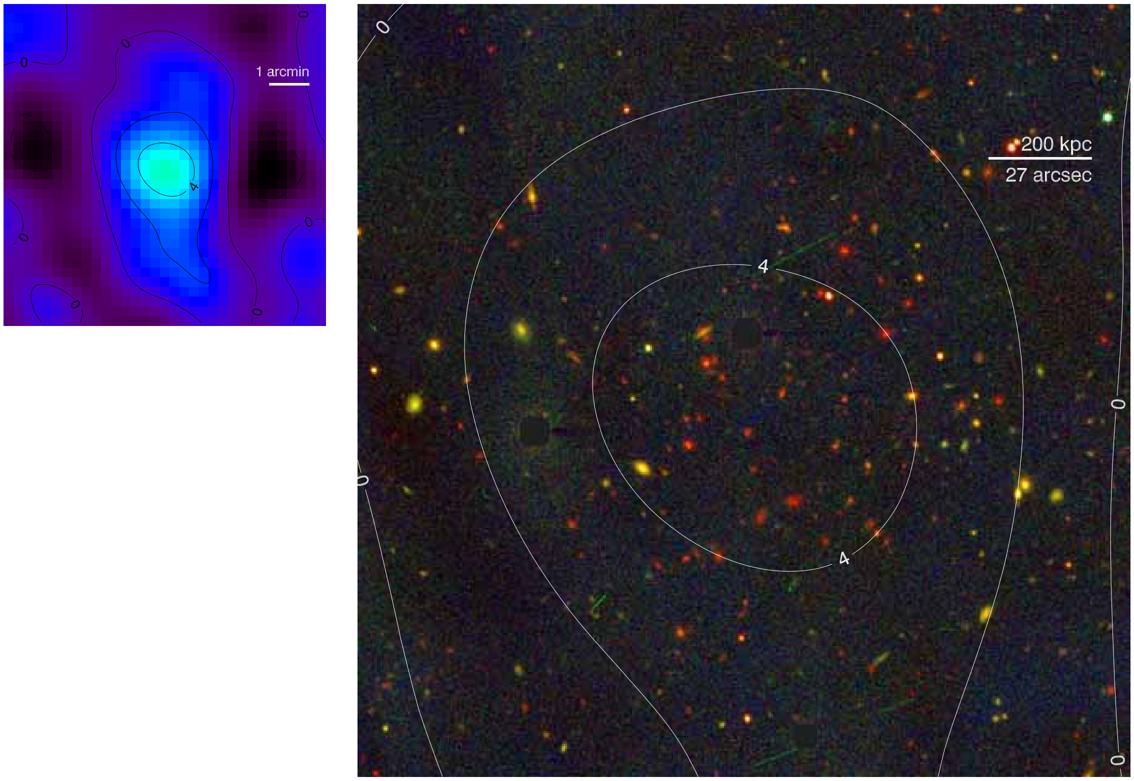

Fig. 19.— SPT-CL J2301-5546

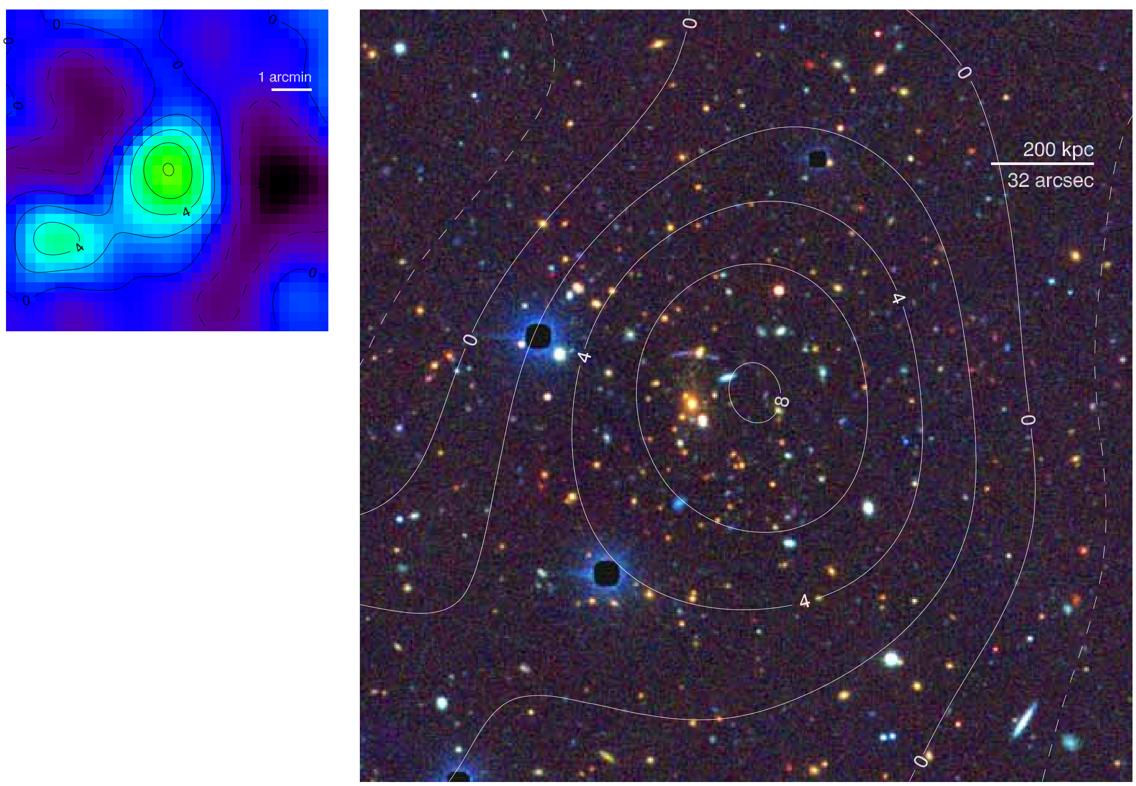

Fig. 20.— SPT-CL J2331-5051

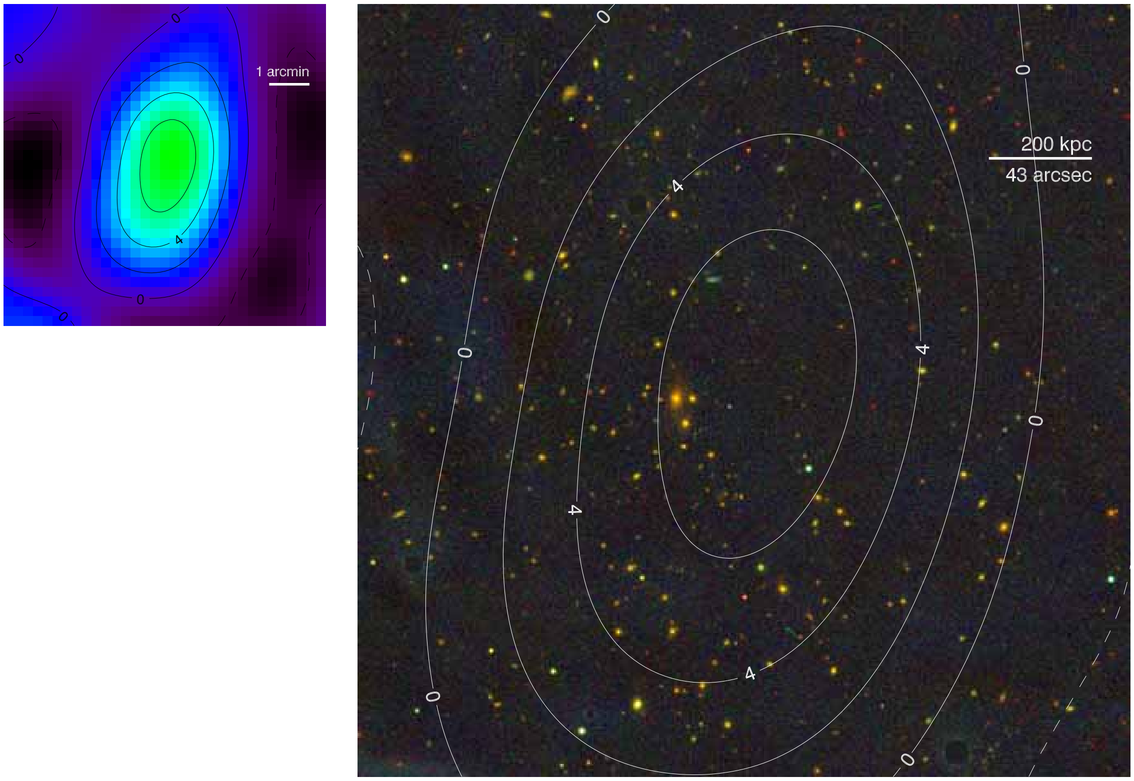

FIG. 21.— SPT-CL J2332-5358

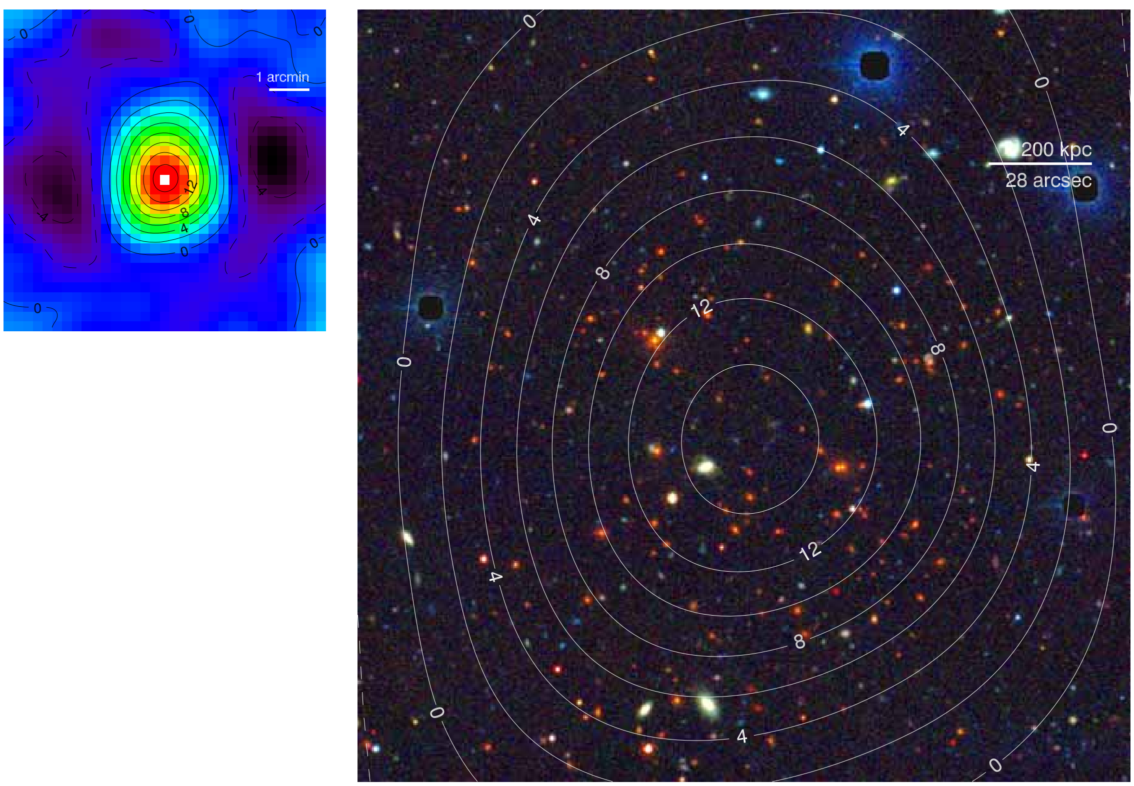

FIG. 22.— SPT-CL J2337-5942

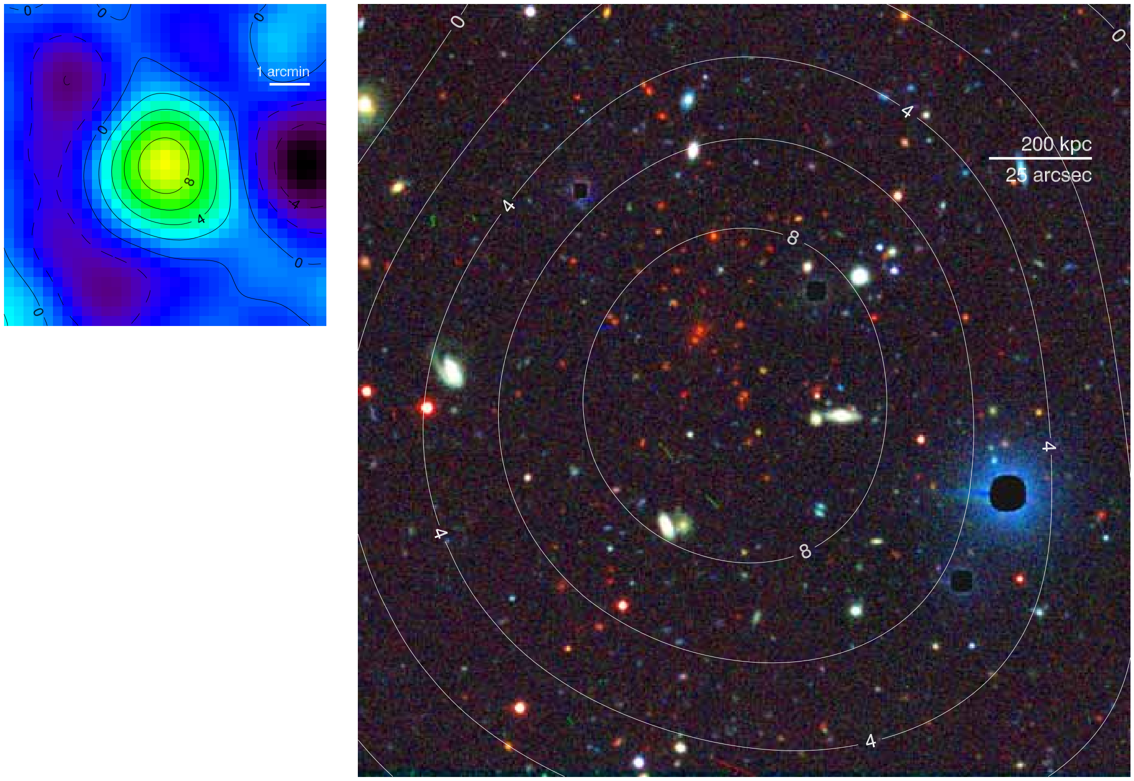

FIG. 23.— SPT-CL J2341-5119

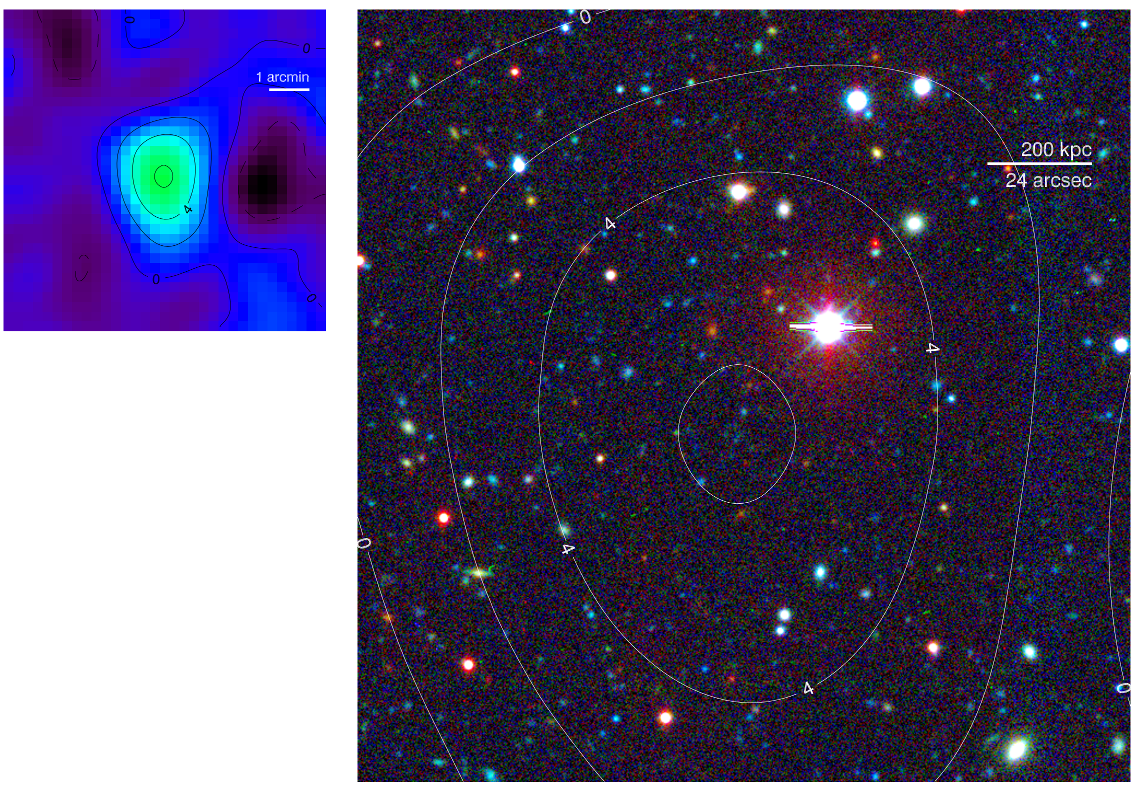

FIG. 24.— SPT-CL J2342-5411

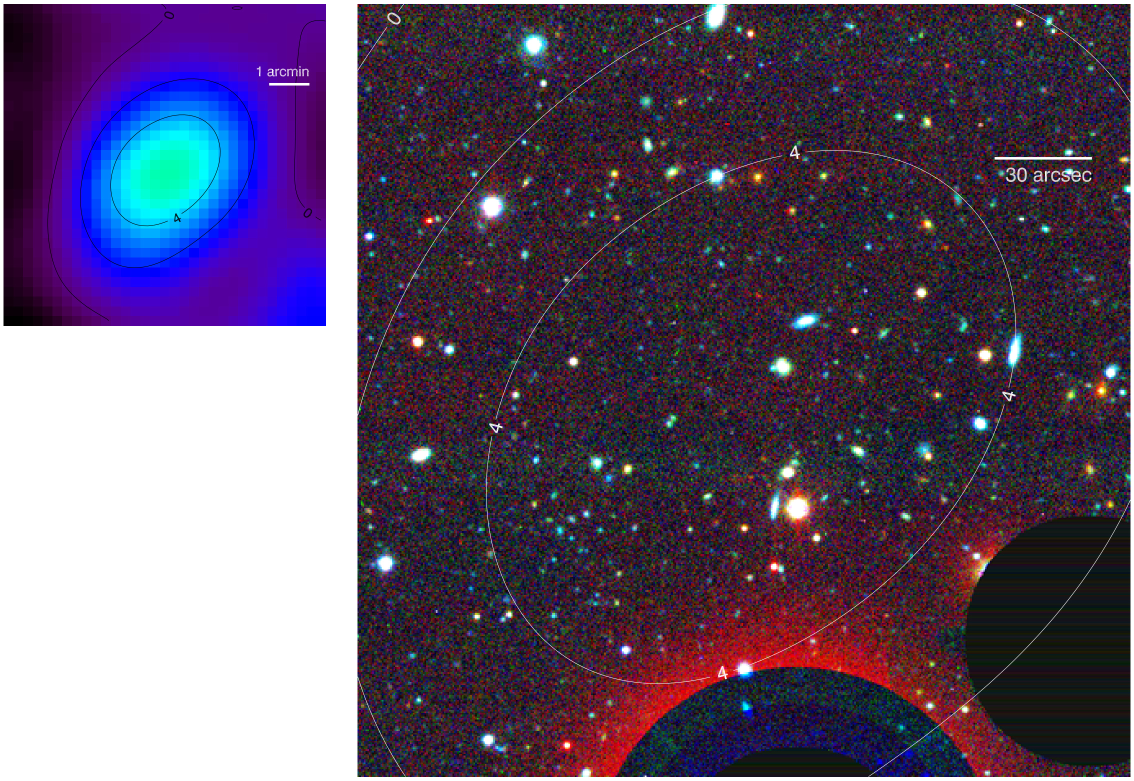

FIG. 25.— SPT-CL J2343-5521 (unconfirmed)

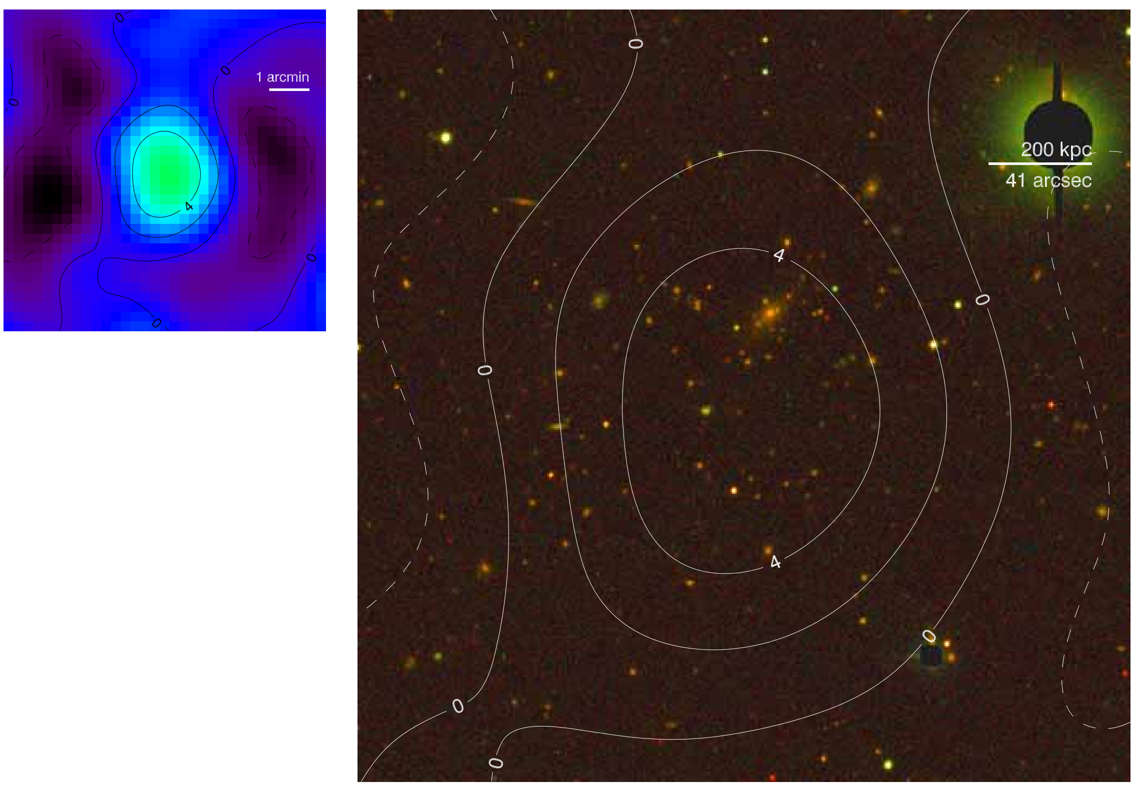

FIG. 26.— SPT-CL J2355-5056

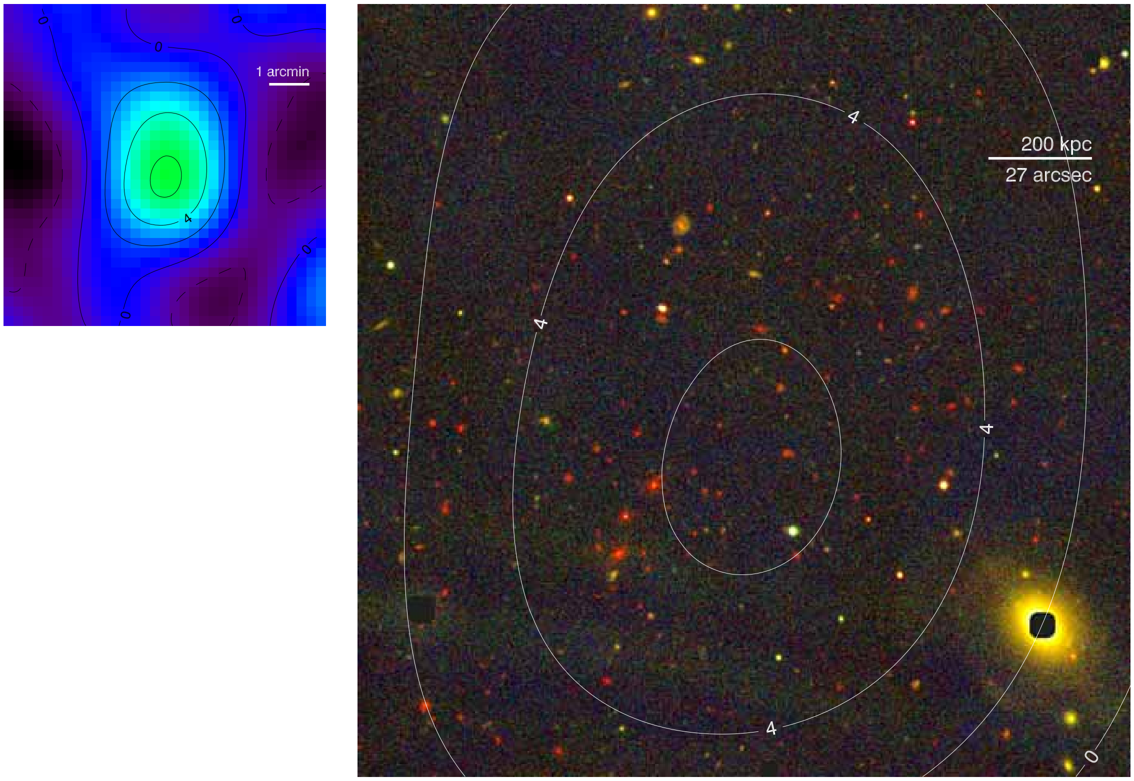

Fig. 27.— SPT-CL J2359-5009

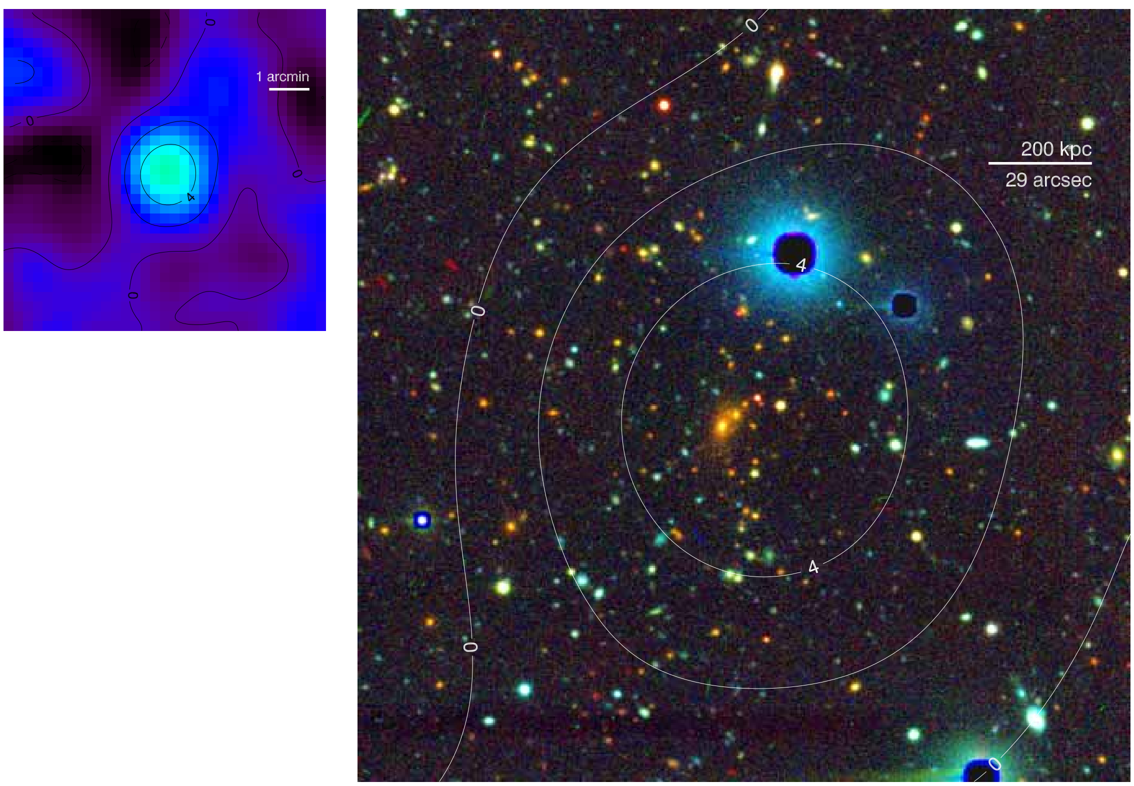

Fig. 28.— SPT-CL J0000-5748